ALMA MATER STUDIORUM · UNIVERSITY OF BOLOGNA

School of Science
Department of Physics and Astronomy
Master Degree in Physics

THICKNESS EFFECTS ON ELECTROCHEMICAL AND GAS-PHASE HYDROGEN LOADING IN MAGNESIUM THIN FILMS

Supervisor: Submitted by:

Prof. Luca Pasquini   Giorgia Guardi

Co-supervisors:

Prof. Astrid Pundt,

Dr. Stefan Wagner

Academic Year 2020/2021

Abstract

Renewable hydrogen is one of the tools necessary to reduce carbon emissions and achieve climate neutrality by 2050, so its production and consumption is planned to increase in the following 30 years. Developing new techniques for hydrogen storage is thus extremely relevant at the moment. Magnesium is a good candidate for hydrogen storage in solids due to its light weight, abundance, safety of operation and high achievable hydrogen density. However, the Magnesium-Hydrogen system needs to be investigated and understood more deeply.

This work focuses on the behaviour of hydrogen in magnesium thin films, using the techniques of electrochemical loading in KOH and gas-phase loading. The formation of magnesium hydride was studied by measuring and comparing isotherm curves. With electrochemical loading it was possible to observe different behaviours during magnesium hydride formation, related to the intensity of the applied driving force. Both hydrogen loading techniques allowed to observe effects related to the thickness of the Magnesium layer. In particular, the voltage or pressure at which Magnesium hydride is formed increases as the film gets thinner.

Contents

Introduction

Renewable hydrogen is one of the tools necessary to reduce carbon emissions and achieve climate neutrality by 2050, reaching the goal set in the *European Green Deal*. As stated in the European hydrogen strategy, investments are planned to upscale the production and consumption of renewable hydrogen in the following 30 years. The objective is to increase production up to 10 million tonnes of renewable hydrogen and to extend its use in fields that are hard to decarbonize, such as the industrial and transport sectors. In this perspective, the development of new techniques for hydrogen storage becomes extremely relevant. Magnesium is a good candidate for hydrogen storage in solids due to its light weight, abundance, safety of operation and high achievable hydrogen density. However, the Magnesium-Hydrogen system needs to be investigated and understood more deeply.

As Hydrogen enters Magnesium new phases with a high hydrogen concentration, known as the hydrides, are created. Hydride formation can be observed as a plateau in pressure-concentration (or equivalent) isotherm curves, and also indirectly because of the associated metal-to-insulator transition. This work focuses on hydride formation in Magnesium thin films, which was investigated by measuring and comparing isotherm curves. The controlled loading of hydrogen in Magnesium was performed with two methods: via electrochemical reactions in KOH and from the gas phase. While gas-phase loading is a widely established method, electrochemical loading in KOH is a less mature technique which required preliminary studies to understand the behaviour of the electrolyte and to perfect the experimental setup. Once that was achieved, possible thickness effects were investigated by comparing the behaviour of the Magnesium-Hydrogen system for three different thicknesses of the Magnesium layer ($\sim$13nm, $\sim$26nm and $\sim$39nm). To prevent oxidation, the samples were covered in Palladium, which can influence the behaviour of the system by alloying with Magnesium. Alloying effects were investigated by surrounding the Magnesium layer with two thin layers of Titanium.

This thesis is structured in four chapters. Chapter 1 deals with the theoretical background necessary to understand the behaviour of hydrogen in metals such as Magnesium and Palladium, highlighting the differences between bulk metals and thin films. Chapter 2 details the experimental methods, including samples' preparation and hydrogen loading techniques. Chapter 3 exposes the main results, including alloying and thickness effects. Finally, Chapter 4 interprets and discusses the obtained results, while comparing the two different methods employed for hydrogen loading.

1. Motivation and theoretical background

1.1. Hydrogen as an energy carrier and hydrogen storage

As acknowledged in the *European Green Deal* [1], renewable hydrogen is one of the tools necessary to reach climate neutrality by 2050, together with the process of electrification and the use of energy from renewable sources.

Hydrogen does not emit CO_2 when used; however, at the present moment, the majority of hydrogen in the European market is produced from fossil fuels and thus introduces air pollution and contributes to global warming. Renewable hydrogen is defined as hydrogen produced by water electrolysis, using energy from renewable sources: in this way, the greenhouse gas emission during production is close to zero. Hydrogen is a good candidate for a clean and cost-efficient fuel also because it is abundant and light, it has the highest known energy contents (see Table 1.1.1) and it is non-toxic.

For this reasons – as stated in *A hydrogen strategy for a climate-neutral Europe* issued by the European Commission in July 2020 [3] – European institutions are determined to boost the supply and demand of renewable hydrogen by 2050. The process will unravel in three phases:

(1) 2020-2024: Decarbonization of hydrogen production for the current uses. The objective is to install 6GW of renewable hydrogen electrolysers and to produce up to 1 million tonnes of renewable hydrogen.
(2) 2024-2030: Extension of hydrogen usage in new sectors. This requires to install at least 40GW of renewable hydrogen electrolysers and to produce up to 10 million tonnes of renewable hydrogen.
(3) 2030-2050: Extension of hydrogen usage to all hard-to-decarbonize sectors.

In the first phase renewable hydrogen will be employed in industrial applications such as steel making, refineries, production of ammonia and methanol. From the second phase

TABLE 1.1.1. Comparison of energy contents of some fuels [2].

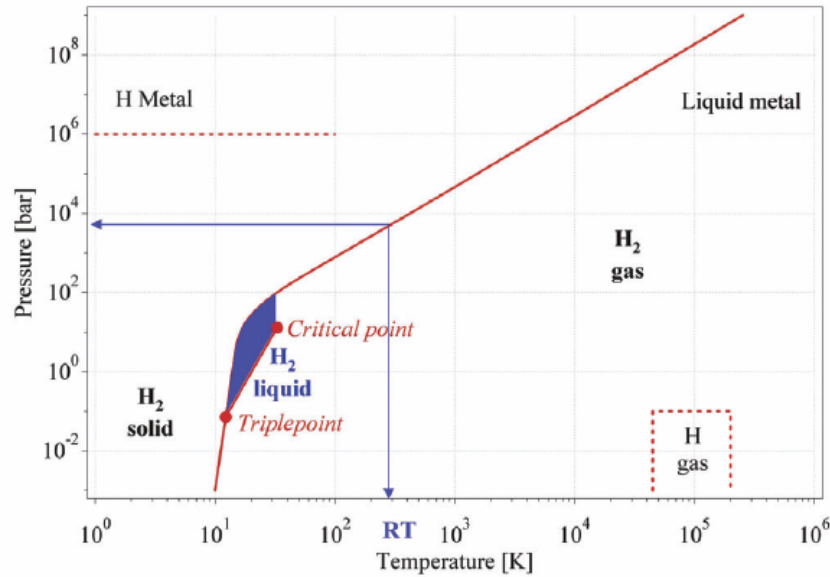| Fuel	Energy content (MJ/kg)
Gaseous hydrogen	119.96
Liquid hydrogen	120.04
Natural gas	47.13
Crude oil	42.68
Liquefied Petroleum Gas (LPG)	46.60
Conventional gasoline	43.44
Reformulated or Low-Sulfur Gasoline (RFG)	42.35
Conventional diesel	42.78
Bituminous coal (wet basis)	26.12
Methanol	20.09
Ethanol	26.95

FIGURE 1.1.1. Hydrogen's phase diagram. RT indicates the room temperature condition, while the blue area identifies liquid hydrogen [**4**].

on, new applications of hydrogen as fuel will be promoted, especially in the transport sector. The city mobility will be addressed first, involving city buses, rail network and commercial fleets (taxis, for example). Heavy-duty road vehicles and trains will follow, since 46% of train railways in Europe are still not electrified and thus rely on Diesel fuel. Further applications will involve waterways, short-sea shipping and, in a more distant future, aviation and maritime shipping; the latter applications will however face higher technical difficulties related to refueling.

In this context, the problem of hydrogen storage becomes extremely relevant. Figure 1.1.1 shows the phase diagram of hydrogen. The small area where hydrogen is in the liquid state is highlighted in blue; the liquid state is observed only at temperatures between those of the triple point and of the critical point. At ambient temperature and pressure however hydrogen is a bi-atomic gas with a low volumetric density: $1kg$ of gas occupies $11m^3$. To store hydrogen efficiently its density has to be decreased, this can be achieved by increasing the pressure, by cooling the gas to create liquid hydrogen or by using the interaction with other materials. In evaluating storage methods we have to take into account the volumetric density (mass of hydrogen per unit volume), the gravimetric density (mass of hydrogen over the total mass, usually expressed in percentage) and also the reversibility of the process, since ideally we want to use all the hydrogen that has been stored. Other relevant parameters, especially for mobile applications, are the working temperature and pressure. Some of the most common methods for hydrogen storage are:

- **High pressure gas cylinders**. This is the most common method for hydrogen storage. The achievable volumetric density depends on the tensile strength of the material and it can be up to $36kg/m^3$ [**4**]. Usually though, a high volumetric

TABLE 1.1.2. Comparison of different hydrogen storage methods based on the gravimetric density ρ_m, volumetric density ρ_V, working temperature and pressure [4]. RT stands for room temperature.

Storage method	$\rho_m(mass\%)$	$\rho_V(kg/m^3)$	$T(°C)$	$p(bar)$
High pressure gas cylinders	13	< 40	RT	800
Liquid hydrogen	size dependent	70.8	-252	1
Metal hydrides	∼ 2	150	RT	1
Complex hydrides	< 18	150	> 100	1

density will decrease the gravimetric density because thicker and heavier walls are necessary to allow an higher internal pressure.

- **Liquid hydrogen**. Liquid hydrogen is created with the Linde cycle, after precooling the gas with liquid nitrogen, and it is then conserved at 21.1K at ambient pressure. Due to the higher energy consumption this process is not competitive with other storage methods. On top of that, part of the hydrogen is continuously lost in evaporation [4].
- **Physisorption**. This method relies on the adsoption of hydrogen at the surface of a material, mediated by Van der Waals forces. Nanosized carbon structures such as carbon nanotubes are generally employed for physisorption [4].
- **Hydrides**. This method is based on hydrogen absorption in metals, followed by the formation of hydrogen-rich phases, known as hydrides. This is the main focus of this work so thermodynamics and kinetics aspects of hydrogen absorption and hydride formation in metals will be discussed in detail in the following paragraphs. The gravimetric density can be increased by employing complex hydrides with lightweight materials [4].

Some relevant parameters for these methods are compared in Table 1.1.2. As we can see hydrides can offer good volumetric and gravimetric densities at ambient pressure and temperature, and are therefore of great interest in the development of hydrogen storage methods for new applications.

This work will mainly focus on hydride formation in Magnesium thin films, comparing two different techniques to load hydrogen in the films and investigating how the behaviour changes with the film's thickness. Within the storage methods based on hydrides, Magnesium has been given particular attention with a growing number of results and publications. This metal is interesting for its high abundance and low costs of production. It is also non-toxic and relatively safe to operate when the hydride is formed by interaction with hydrogen gas or through electrochemical reactions. Due to its light weight and large stoichiometric hydrogen storage capacity it provides a high gravimetric density of $7.6mass\%H$ and an acceptable volumetric density of of $110kgH/m^3$ [5]. However, Mg has several drawbacks as a hydrogen storage material. Firstly, the hydride phase forms at low pressures; this means that at normal pressures a very high temperature is necessary for the hydrogen to leave the material, which is incompatible with most practical applications. The second aspect is related to its low rate of interaction with hydrogen gas. As will be discussed in the following paragraphs many mechanisms could be responsible for the slow kinetics, the main one probably being the slow diffusion of

hydrogen in the hydride phase. These problems can be partially solved by nanostructuring, which destabilized the system by increasing the equilibrium pressure and at the same time provides faster routes for diffusion, other techniques involve alloying with other elements or various mechanical treatments.

1.2. Basic aspects of Hydrogen-Metal systems

This section deals with some fundamental aspects that are necessary to understand the hydrogen-metal system: how hydrogen is adsorbed at the metal surface and then absorbed into the metal (paragraph 1.2.1), how hydrogen behaves once inside the metal (paragraph 1.2.2) and the effects of hydrogen absorption on the host metal's crystal lattice (paragraph 1.2.3).
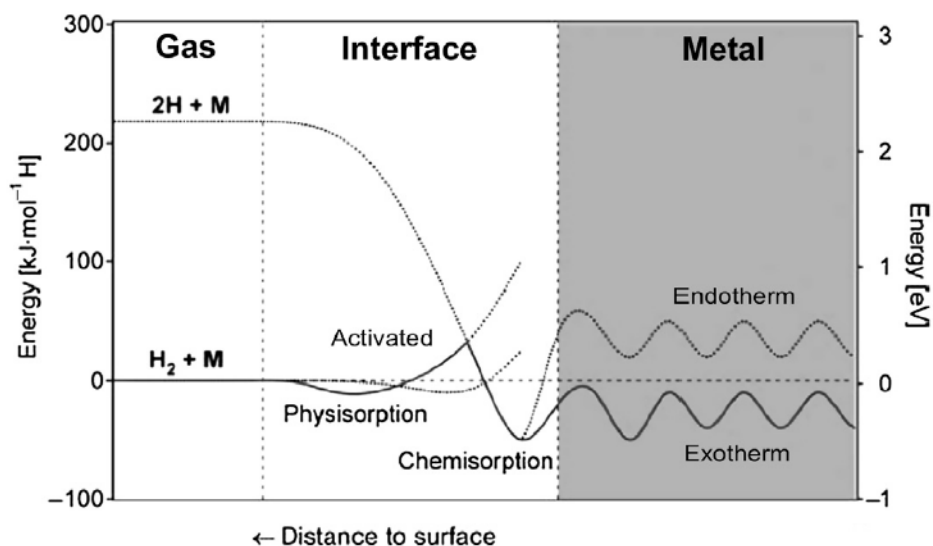

FIGURE 1.2.1. Labelled as $H_2 + M$: potential describing the interaction between an hydrogen molecule and metal atoms as a function of the distance from the surface. Labelled as $2H + M$: potential of the interaction between two single hydrogen atoms and metal atoms at the surface and in the bulk of the metal. On the right side two different scenarios are represented, depending on whether the H absorption is endotherm or exotherm. The difference between the two curves far from the surface (on the left side) corresponds to the dissociation energy for the H_2 molecule [6].

1.2.1. Hydrogen adsorption and absorption. Hydrogen intake in metals begins at the surface, where an hydrogen molecule H_2 can interact with the metal's surface atoms through Van Der Waals forces. This first step is called physisorption because it is only mediated by attractive dipole-dipole interactions and thus it doesn't involve the dissociation of the molecule. The Lennard-Jones potential for this type interaction is represented on the left side on Figure 1.2.1, together with the energy necessary to dissociate the H_2 molecule and create a bond with the surface atoms. The bond between

single H atoms and surface atoms is called chemisorption and it becomes energetically favourable as we get closer to the surface, even though it might be necessary to overcome a potential barrier in the case of an activated process. H absorption in the bulk of the metal can follow from chemisorption, if the process is exotherm.

Depending on the temperature and on the orientation of the surface, H adsorption shows different phases, which are mainly characterized by the surface coverage. For instance, Pd(100) and Pd(111) exhibit a surface coverage of $\sim 1H/Pd$ at room temperature, but this value can increase up to $1.5H/Pd$ at lower temperatures [6].
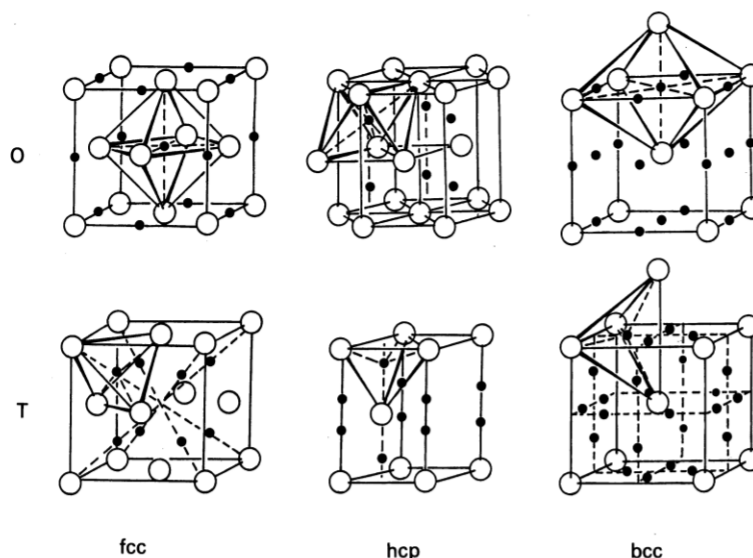

FIGURE 1.2.2. Representation of Octahedral (O) and Tetrahedral (T) interstial sites for body centered cubic (bcc), face centered cubic (fcc) and hexagonal close packed (hcp) crystals [7].

TABLE 1.2.1. Space group and lattice parameters for pure element, solid solution and hydride phases of Mg [10] and Pd [11].

Phase	Space group	Lattice parameter (nm)		
		a	b	c
Mg	$P6_3/nmc$	0.32	0.32	0.52
α	$P6_3/nmc$	0.32	0.32	0.52
β	$P4_2/mnm$	0.45	0.45	0.30
Pd	$Frn3m$	0.388874	-	-
α	$Frn3m$	0.3895	-	-
α'	$Frn\bar{3}m$	0.4025	-	-

1.2.2. The solid solution and the hydride phase. As they move away from the surface and make their way into the bulk of the system, due to their small volume, H atoms will occupy interstitial sites in the metal's crystal structure. As an example, figure
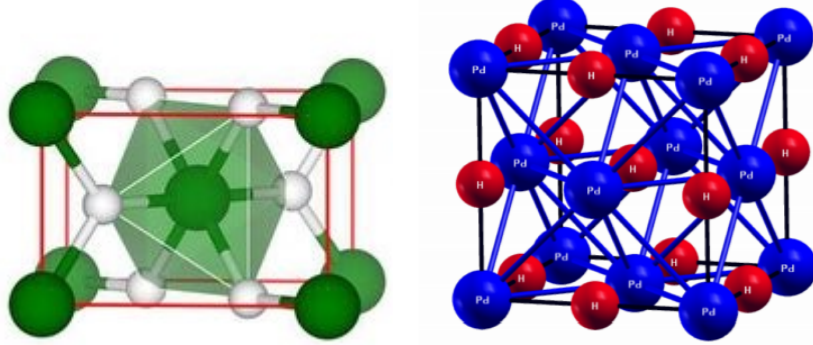
FIGURE 1.2.3. On the left: crystal structure of MgH_2 (Mg in green and H in white) [8]. On the right: crystal structure of PdH (Pd in blue and H in red) [9].

1.2.2 represents Octahedral and Tetrahedral sites for some common crystal structures (bcc, fcc and hcp). Other interstitial sites exist, but they are not represented as they are not large enough to host H atoms. At low concentrations, hydrogen atoms will occupy random interstitial sites in what is called a solid solution. In the case of Magnesium and Palladium, the low quantity of hydrogen in the solid solution does not affect the material's properties. As the concentration increases, new phases known as hydrides form. The hydride is characterized by a modification of the structure of the metal lattice caused by hydrogen absorption [7], and it can have radically different properties from the pure metal. For example MgH_2 – the hydride phases of Mg – is an insulator and thus it has a higher resistance and optical transmittance with respect to pure Magnesium. The higher hydrogen density of the hydride phase can also affect the hydrogen diffusion constant. For example, the diffusion constant of Mg at room temperature drops by 17 orders of magnitude – from $D_H^{Mg} \sim 10^{-10} m^2/s$ to $D_H^{MgH_2} \sim 10^{-27} m^2/s$ – upon hydride formation [5].

In the case of Mg, the pure element and the solid solution, usually indicated as α-phase, exhibit a hcp structure (see Figure 1.2.2) while the hydride, indicated as β-phase, shows a rutile crystal structure (see Figure 1.2.3) [10]. For Pd both the solid solution (α-phase) and the hydride (α'-phase) have a fcc crystal structure, but the hydrogen presence modifies the lattice parameter [11]. The MgH crystal structure is also represented in Figure 1.2.3. Space group and lattice parameters of the presented phases are reported in Table 1.2.1; a more detailed discussion on their relation to H concentration, pressure and temperature will follow.

1.2.3. Lattice expansion. Hydrogen absorption causes a deformation of the crystal lattice. Lattice expansion can be evaluated considering the volume change per absorbed hydrogen atom Δv. The relative variation of the total volume of the metal $\Delta V/V$

after absorbing n_H hydrogen atoms is then given by:

$$\frac{\Delta V}{V} = \frac{n_H \Delta v}{V} = \frac{n_H \Delta v}{N\Omega} = c_H \frac{\Delta v}{\Omega} \tag{1.2.1}$$

where N is the total number of metal atoms, Ω is the mean metal atom volume and c_H is the concentration of hydrogen atoms. Figure 1.2.4 shows that the linear relationship between volume variation and hydrogen concentration holds for different types of fcc metals at concentrations up to $\sim 0.7 H/M$.

Considering a first order approximation, the volume variation can be translated to a length variation and subsequently to a relative variation of the lattice parameter a:

$$\frac{\Delta a}{a} = \frac{1}{3} c_H \frac{\Delta v}{\Omega} \tag{1.2.2}$$

This quantity is of particular interest since it can be measured precisely by XRD and then used to extract $\Delta v / \Omega$. This volume variation upon hydrogen absorption is 19% for Pd [6] and 30% for Mg [5].
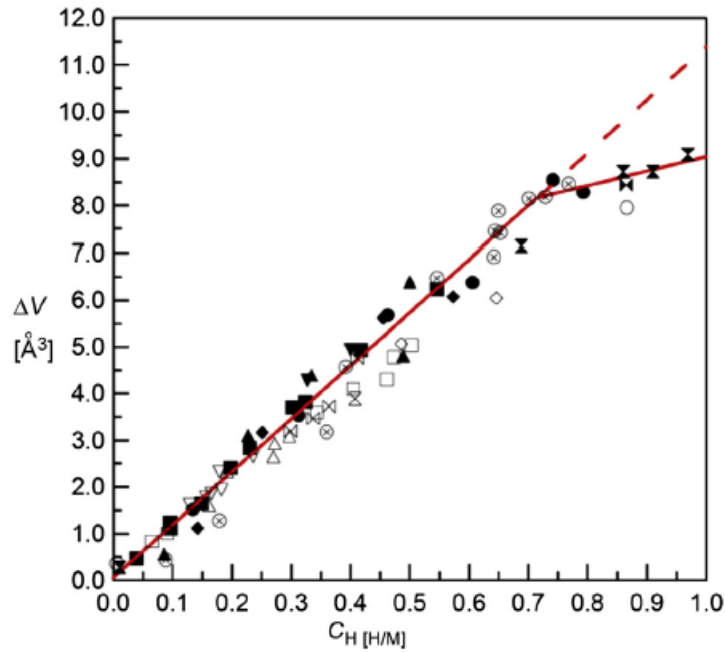

FIGURE 1.2.4. Realtionship between the volume variation and the hydrogen concentration for different fcc metals and alloys ($Pd, Ni, Ir-Pd, Au-Pd, Ag-Pd, Pt-Pd, Cu-Pd$ and $Cu-Ni$) from the work of Baranonwski at al. [12].

1.3. Thermodynamic aspects of the metal-hydrogen system

This section examines some thermodynamics aspects of hydrogen absorption in metals, especially focusing on Magnesium and Palladium. All the results refer to bulk metals; the deviations from this behaviour in thin films will be discussed in a following
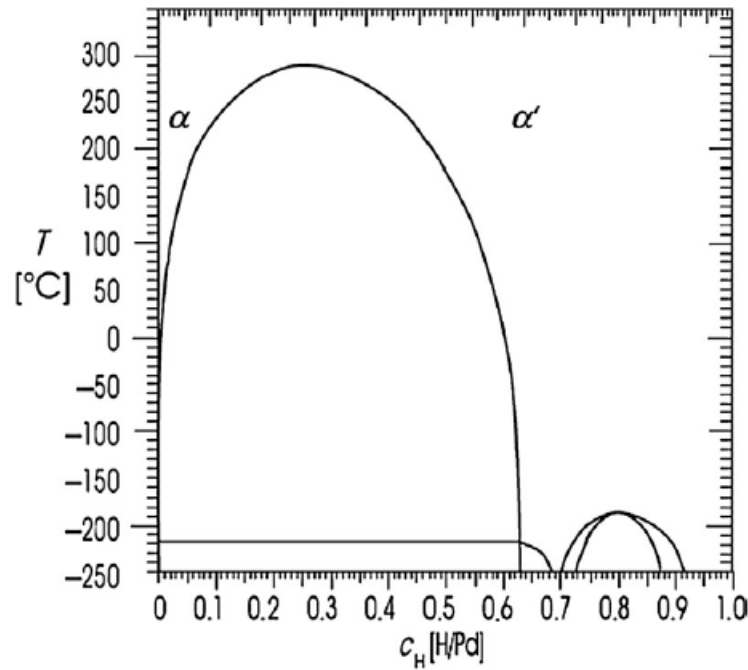
FIGURE 1.3.1. Phase diagram of Pd-H at a pressure of 1 bar [6].

section. Paragraph 1.3.1 deals with $Mg - H$ and $Pd - H$ phase diagrams, describing the conditions to develop the solid solution and the hydride phase and the resulting pressure-concentration isotherms. Paragraph 1.3.2 describes hydrogen absorption at low concentration in the solid solution, while paragraph 1.3.3 deals with the thermodynamics of hydride formation.

1.3.1. Phase Diagrams and Isotherms. Figure 1.3.1 shows the phase diagram for the Pd-H bulk system at a pressure of 1 bar. Except for very low temperatures we find the two phases introduced in paragraph 1.2.2: the solid solution, or α-phase, and the hydride, or α'-phase. The α-phase is the equilibrium state of the system at low hydrogen concentrations, while the α'-phase is the equilibrium phase at higher concentrations. Between those two regions is the miscibility gap, where the two phases coexist at equilibrium over a wide range of hydrogen concentrations. For example, at $25°C$ we have only the α-phase up to a concentration of $0.017 H/Pd$, and only the α'-phase for concentrations larger than $0.60 H/Pd$ [11]; for all the intermediate values both states will be observed at equilibrium. The maximum hydrogen concentration at which the α-phase represents the system's equilibrium state is known as the hydrogen solubility limit; in the case of Pd at $25°C$ it is, as mentioned above, $0.017 H/Pd$. The miscibility gap's size decreases with temperature and eventually disappears at the critical temperature $T_C = 293°C$, where the two phases become indistinguishable. At temperatures below $\sim -220°C$ more phases appear. These phases are related to an ordered distribution of the H atoms in the interstitial sites but are of no interest for the objectives of this work, since all measurements were performed at room temperature.
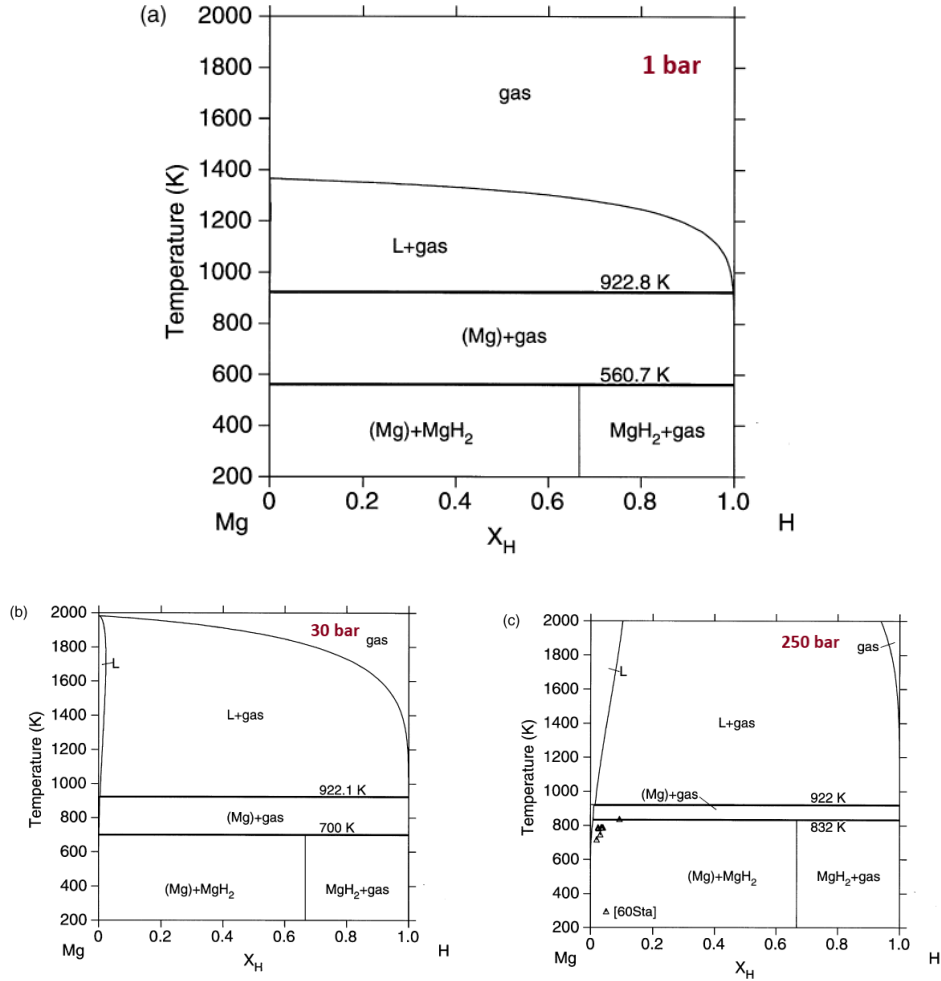
FIGURE 1.3.2. Phase diagram of the Mg-H system at (a) 1bar, (b) 30 bar and (c) 250bar [**13**].

Figure 1.3.2 represents the phase diagram of the $Mg - H$ system at three different pressures (1bar, 30bar and 250bar). Together with the liquid (L in the figure) and the gas phase, the solid solution and the hydride, presented in paragraph 1.2.2, appear on the diagram. Here the solid solution (α-phase) is indicated as (Mg) while the hydride (β-phase) is indicated as MgH_2. Also, the x-axis considers the molar fraction $X_H = n_H/(n_H + N)$ instead of the hydrogen concentration $c_H = n_H/N$. The solubility of hydrogen in magnesium in extremely low; to see the solid solution area we need to focus on a very small portion of the x-axis (Figure 1.3.3) and the highest solubility is $X_H = 7 \times 10^{-4}$, right below the Mg fusion temperature. At 1bar the hydride phase MgH_2 is present only for temperatures below 650.7K, in equilibrium with the solid solution (Mg) or with the gas phase depending on the hydrogen molar fraction. Above this temperature the hydride dissociates in (Mg)+gas. As we can see comparing the three panels in Figure 1.3.2, the temperature for the $MgH_2 \longleftrightarrow (Mg)+gas$ dissociation increases with pressure, while the $L \longleftrightarrow (Mg) + gas$ dissociation temperature is almost
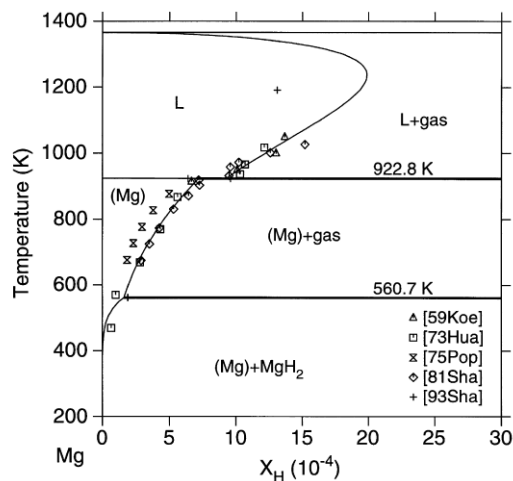
FIGURE 1.3.3. Phase diagram of the Mg-H system at 1bar for low hydrogen concentrations. From Zeng at al. [**13**], compared with the results of other studies.
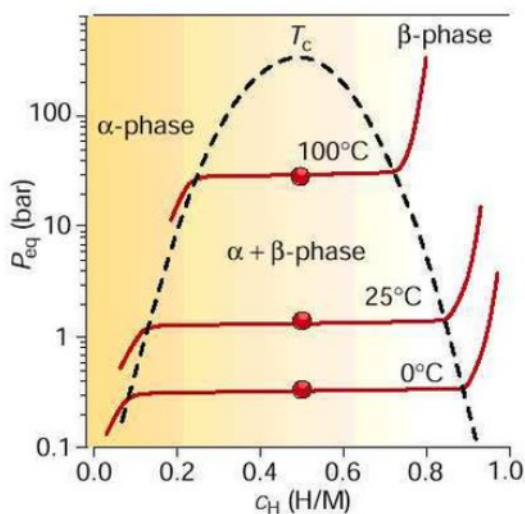
FIGURE 1.3.4. Pressure-concentration isotherms at differents temperatures for a metal-hydrogen systems that presents a miscibility gap [**14**].

constant at $\sim 922K$. Other metastable phases have been reported to appear at high pressures but are of little concern to this work.

Phase diagrams of the kind of Pd and Mg, where two phases are in equilibrium over a certain area, determine a plateau in the pressure-composition isotherms: when the phases are in equilibrium their chemical potential is expected to remain constant, and so will the logarithm of the pressure. Pressure-composition isotherms are in fact used to derive the phase diagrams, since the width of the pressure plateau can be used to

FIGURE 1.3.5. Isotherms for the Palladium-Deuterium system at different temperatures. An hysteresis between loading and unloading curves is visible especially at lower temperatures [7].
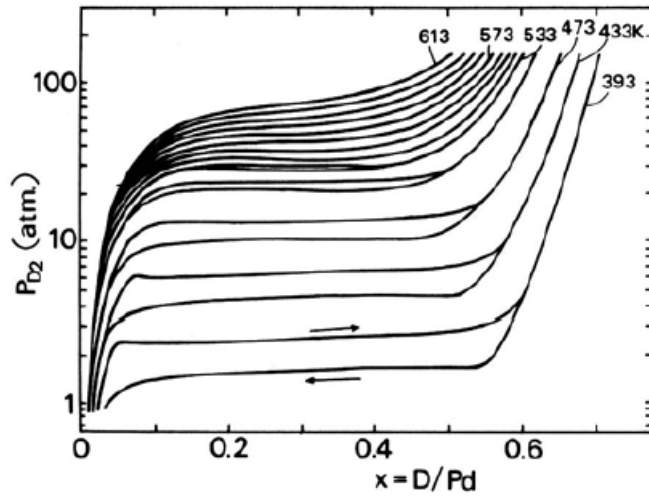
define the boundaries of the miscibility gap. A generic example of this behaviour for a hydrogen-metal systems is reported in Figure 1.3.4.

The isotherms often present an hysteresis, an example is reported in Figure 1.3.5. The equilibrium pressure is usually higher when we start at a low H concentration and gradually increase it to create the hydride (loading), than in the opposite process of starting from the hydride and gradually decreasing the H concentration (unloading). In this case, the unloading plateau is usually considered to construct phase diagrams [13]. The presence of an hysteresis indicates that some energy is dissipated along the process. This is usually attributed to the formation and migration of dislocation as we enter or exit the two-phase region: the different lattice parameter or crystal structure between the two phases (see Table 1.2.1, as an example) creates elastic strain energy, that can be released by forming a dislocation [6].

1.3.2. Sievert's law. The first stages of hydrogen absorption from the gas phase can be described by Sievert's law. The exact expression will be derived in the next paragraph, but essentially it expects the hydrogen concentration in the metal to scale with the square root of the gas pressure: $c_H \propto \sqrt{p_{H_2}}$. This behaviour was first observed by Sievert in 1929 during his studies on gases dissolution in metals.

To derive this equation we will suppose a thermodynamic equilibrium between hydrogen atoms absorbed in the metal and molecules in the gas phase. The condition for thermodynamic equilibrium is that the two phases must have the same chemical potential. The chemical potential for the gas phase is well known and, assuming a perfect gas, is given by:

$$\mu_{H_2}^{gas} = \mu_0 + k_b T ln \left(\frac{p_{H_2}}{p_0} \right) \tag{1.3.1}$$

where μ_0 is the standard chemical potential of the gas phase, accounting for the molecule's dissociation energy and for vibrational contribution to the entropy, $p_0 = 1.013 \times 10^5 Pa$ is the standard pressure for the gas phase and k_b is Boltzmann's constant. The chemical potential also depends on the temperature T and on the gas pressure p_{H_2}.

The chemical potential of absorbed hydrogen atoms can be found as the Gibbs free energy per unit mole:

$$\mu_H^M = \left(\frac{\partial G_H^M}{\partial n_H}\right)_{p,T} \tag{1.3.2}$$

where n_H is the number of hydrogen atoms and G_H^M is the Gibbs free energy. By definition the Gibbs free energy can be written considering enthalpy (H_H^M) and entropy (S_H^M):

$$G_H^M = H_H^M - TS_H^M = H_H^M - T\left(S_H^{conf} + S_H^{exc}\right) \tag{1.3.3}$$

In the second part of the equation we have separated the configurational part of the entropy (S_H^{conf}), that depends on the possible different ways to arrange the n_H hydrogen atoms over the available n_i interstitial sites, from the rest of the entropy (S_H^{exc}) that is due to vibrational and electronic contributions. Considering Boltzmann's definition of entropy, S_H^{conf} can be written considering the binomial coefficient of n_i and n_H, which represents the number of ways in which we can arrange the hydrogen atoms in the available interstitial sites.

$$S_H^{conf} = k_b ln\left(\frac{n_i!}{n_H!(n_i - n_H)!}\right) \tag{1.3.4}$$

Using Stirling's approximation $lnx! \simeq xlnx - x$, we can expand the equation as:

$$\begin{aligned} S_H^{conf} &= k_b\left(n_i lnn_i - n_i - (n_i - n_H)ln(n_i - n_H) + n_i - n_H - n_H lnn_H + n_H\right) \\ &= k_b\left(n_i ln\left(\frac{n_i}{n_i - n_H}\right) - n_H ln\left(\frac{n_H}{n_i - n_H}\right)\right) \end{aligned} \tag{1.3.5}$$

and we can derive Eq. (1.3.5) with respect to n_H:

$$\begin{aligned} \frac{\partial S_H^{conf}}{\partial n_H} &= k_b\left(\frac{n_i}{n_i - n_H} - lnn_H - 1 + ln(n_i - n_H) - \frac{n_H}{n_i - n_H}\right) \\ &= k_b ln\left(\frac{n_i - n_H}{n_H}\right) \end{aligned} \tag{1.3.6}$$

At this point we can finally write an expression for the chemical potential of the hydrogen atoms absorbed in the metal:

$$\mu_H^M = h_H^M - Ts_H^{exc} + k_b Tln\left(\frac{n_H}{n_i - n_H}\right) \tag{1.3.7}$$

By dividing numerator and denominator of the logarithm argument in the previous equation by the total number N of metal atoms we introduce the hydrogen concentration $c_H = n_H/N$ and the interstitial sites fraction $r = n_i/N$, obtaining:

$$\mu_H^M = h_H^M - Ts_H^{exc} + k_b Tln\left(\frac{c_H}{r - c_H}\right) \tag{1.3.8}$$

The value of r depends on the metal's crystal structure, for example Pd with its fcc structure has $r = 1$.

The last step consists in equating the chemical potentials. The gas chemical potential (Eq. (1.3.1)) will have to be divided by two since it refers to an hydrogen molecule composed by two individual atoms.

$$
\begin{aligned}
\frac{\mu_0}{2} + \frac{k_b T}{2} ln\left(\frac{p_{H_2}}{p_0}\right) &= h_H^M - T s_H^{exc} + k_b T ln\left(\frac{c_H}{r - c_H}\right) \\
k_b T \left(ln\sqrt{\frac{p_{H_2}}{p_0}} - ln\left(\frac{c_H}{r - c_H}\right)\right) &= h_H^M - T s_H^{exc} - \frac{\mu_0}{2} \\
\frac{r - c_H}{c_H}\sqrt{\frac{p_{H_2}}{p_0}} &= exp\left(\frac{1}{k_b T}\left(h_H^M - T s_H^{exc} - \frac{\mu_0}{2}\right)\right) \\
\frac{c_H}{r - c_H} &= \sqrt{\frac{p_{H_2}}{p_0}} exp\left(-\frac{1}{k_b T}\left(h_H^M - T s_H^{exc} - \frac{\mu_0}{2}\right)\right)
\end{aligned}
\tag{1.3.9}
$$

Considering a small concentration of hydrogen, so that $c_H << r$, the left part of the previous equation can be approximated as $c_H/(r - c_H) \approx c_H$, giving the final result for Sievert's law:

$$
c_H = \sqrt{\frac{p_{H_2}}{p_0}} exp\left(-\frac{1}{k_b T}\left(h_H^M - T s_H^{exc} - \frac{\mu_0}{2}\right)\right)
\tag{1.3.10}
$$

As stated at the beginning of the paragraph, hydrogen concentration in the metal is proportional to the square root of the hydrogen gas pressure. This relationship derives from diving in half the gas chemical potential when imposing the equilibrium condition (Eq. (1.3.9)), so it is caused by the biatomic nature of the hydrogen gas. Similar relationships are observed for other biatomic gases such as oxygen and nitrogen – of course the argument of the logarithm, that contains the difference between standard chemical potentials in gas and in the solid solution, will have different values. For monoatomic gases, like helium or neon, we will instead observe a linear relationship between concentration in the metal and gas pressure; this also applies when gas molecules dissolve into a solid without dissociating. The approximation of a small concentration with respect to the interstitial sites fraction r is usually valid for a very small interval; in the case of Pd, where $r = 1$, Sievert's law is experimentally observed up to a concentration of $x = 0.006 H/Pd$ [11].

The heat of solution is defined as the the enthalpy variation during hydrogen absorption: $\Delta h_H^{M-gas} = h_H^M - 1/2 h_H^{gas}$. At low concentrations it is given by [7]:

$$
\Delta h_H^{M-gas} = \frac{\partial ln c_H}{\partial(1/k_b T)}
\tag{1.3.11}
$$

Figure 1.3.6 shows the dependence of the heat of solution on the hydrogen concentration for different metals. The curves show a common trend: the heat of solution decreases at first with the concentration and then increases again. This can be explained considering H-H interactions. In particular the initial decrease is explained by average elastic interaction, while the increase is due to electronic effects. The hydrogen atoms introduce extra
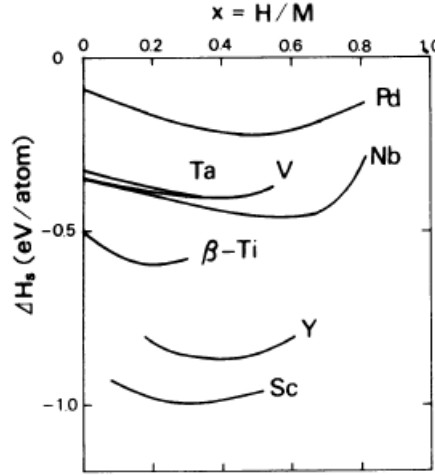
FIGURE 1.3.6. Heat of solution for hydrogen in different metals as a function of its concentration. The heat of solution tends to decrese at first and then increase again [**7**].

electrons that will occupy the metal's energy levels, thus increasing its Fermi energy and the heat of solution. This effect is particularly strong when the Fermi levels lies close to a low-density part of the energy spectrum [**6**].

1.3.3. Hydride formation. As the hydride phase forms, the conditions for equilibrium become more complicated with respect to the one considered in the previous paragraph to derive Sievert's law. When we are in the miscibility gap two phases will coexist in the solid, with different hydrogen concentrations c_α (solid solution) and c_β (hydride); the value of c_β will be somehow close to the stoichiometry value (for example $\sim 2H/Mg$ for MgH_2). The two phases also need to be in equilibrium with the gas phase. The hydride formation from the α-phase in a generic metal M can be described by the reaction:

$$\frac{1}{c_\beta - c_\alpha} MH_{c_\alpha} + \frac{1}{2}H_2 \longrightarrow \frac{1}{c_\beta - c_\alpha} MH_{c_\beta} \tag{1.3.12}$$
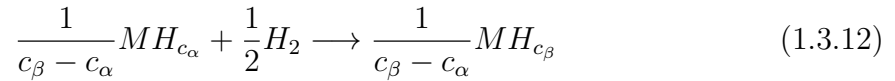
Considering the enthalpy and entropy variations in the reaction the equilibrium condition is simply given by:

$$\Delta h^{\alpha \to \beta} - T\Delta s^{\alpha \to \beta} = 0 \tag{1.3.13}$$

If we consider the chemical potential the equilibrium conditions between the two phases in the solid and the gas phase are given by [**7**]:

$$\mu^\alpha(p, T, c_\alpha) = \mu^\beta(p, T, c_\beta) = \frac{1}{2}\mu^{gas}(p, T) \tag{1.3.14}$$

$$\mu_0^\alpha(p, T, c_\alpha) = \mu_0^\beta(p, T, c_\beta) \tag{1.3.15}$$

where μ_0 represents the chemical potential when the hydrogen concentration is zero, so the chemical potential of the metal species. Since we have three equations, only one between the four variables p (pressure), T (temperature), c_α and c_β will be independent from the others.
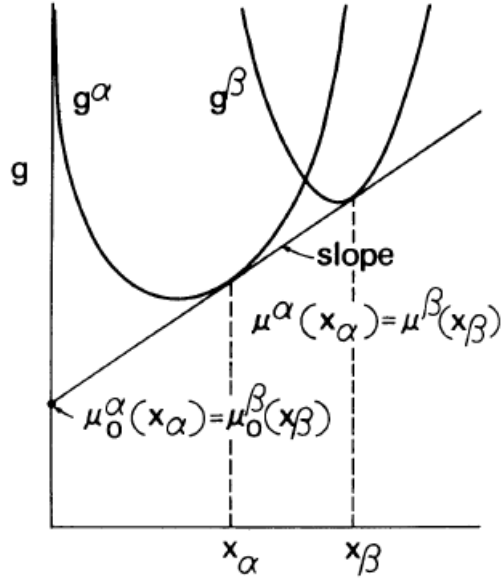
FIGURE 1.3.7. Common tangent construction for an example metal-hydrogen system. g^α represents the free energy for the solid solution, while g^β is the free energy for the hydride. The hydrogen concentration at equilibrium is x_α in the α-phase and x_β in the β-phase since at these two points the free energy curves have the same derivative and thus the same chemical potential (see Eq. (1.3.14)). Also the second equilibrium condition (Eq. (1.3.15)) is satisfied since the two tangents intercept the y-axis at the same point [7].

These conditions for equilibrium can be visualized with the common tangent construction, considering the relationship between chemical potential and free energy introduced in Eq. (1.3.2). This can further be elaborated as:

$$\mu_H = \left(\frac{\partial G}{\partial n_H}\right)_{p,T} = \left(\frac{\partial g}{\partial c_H}\right)_{p,T} \tag{1.3.16}$$

where g is the Gibbs free energy per metal atom. This means that, at a certain pressure and temperature, the equilibrium conditions are met for concentrations that yield the same derivative of the free energy curves of the two phases, as we can see in figure 1.3.7. In reference to this figure the chemical potential at equilibrium can also be written as:

$$\mu^\alpha(c_\alpha) = \mu^\beta(c_\beta) = \frac{g^\beta(c_\beta) - g^\alpha(c_\alpha)}{c_\beta - c_\alpha} \tag{1.3.17}$$

Considering an explicit expression for the gas chemical potential (see Eq. 1.3.1) the first equilibrium condition becomes:

$$\frac{1}{2}ln\left(\frac{p_{eq}}{p_0}\right) = \frac{1}{k_bT}\left(\mu^\alpha - \frac{1}{2}\mu_0^{gas}\right) = \frac{1}{k_bT}\left(\mu^\beta - \frac{1}{2}\mu_0^{gas}\right) \tag{1.3.18}$$

TABLE 1.3.1. Plateau pressure at 25°C, enthalpies and entropies of formation for Mg and Pd hydrides [**6**].

	$p_{eq}(mbar)$	$\Delta H^{\alpha-\beta}(kJ/molH_2)$	$\Delta S^{\alpha-\beta}(kJ/K-molH_2)$
$Mg-MgH_2$	1.1×10^{-3}	-74.5	-0.135
$Pd-PdH_{0.6}$	83	-41.0	-0.0976

Comparing this result to the reaction for the hydride formation (Eq 1.3.12) we can see that the enthalpy and entropy changes in passing from the α to the β phase correspond to the enthalphy and entropy of formation of the two phases at the equilibrium concentration. Values for the equilibrium pressure (in bulk), together with enthalpy and entropy variation when passing from the solid solution to the hydride are reported in Table 1.3.1.

1.4. Hydrogen in Metal Thin Films

The results discussed so far all refer to hydrogen in bulk metals. This section will illustrate the behaviour of hydrogen in metal thin films, highlighting the differences from the bulk case. Those differences are mainly due to defects and surface effects and to mechanical stress following hydrogen absorption.

1.4.1. Equilibrium pressure variation in metal thin films. The higher surface to volume ratio in thin films with respect to bulk metals can destabilize the system by increasing the pressure for hydride formation, if the hydride has a higher interface energy with respect to the pure metal. The following paragraph discusses the position of the hydride formation plateau pressure in Magnesium films of different thicknesses, but similar considerations can be extended to other metals.

Neglecting the solubility in the α-phase the reaction for hydride formation (Eq. 1.3.12) becomes:

$$\frac{1}{c_\beta}M + \frac{1}{2}H_2 \longrightarrow \frac{1}{c_\beta}MH_{c_\beta} \tag{1.4.1}$$

In the case of Mg $c_\beta = 2$ so we will consider the reaction:

$$Mg + H_2 \longrightarrow MgH_2 \tag{1.4.2}$$

The equilibrium pressure for this process in bulk Magnesium $p_{H_2}^{bulk}$ is given by [**15**]:

$$ln\left(\frac{p_{H_2}^{bulk}}{p_0}\right) = \frac{1}{RT}\Delta_f G^0_{MgH_2} \tag{1.4.3}$$

where R is the universal gas constant, T is the temperature and $\Delta_f G^0_{MgH_2}$ is the Gibbs free energy variation upon hydride formation. Considering now a thin film of Magnesium we will have to add to the free energy for hydride formation a second contribution, related to the interface energy γ. In particular we have to consider the interface energy variation between pure Mg and MgH_2, and sum it for the different interfaces present in the sample (for example with pure Mg, with the substrate and with the capping layer for the different crystal orientations). Adding this contributions we obtain for the equilibrium pressure
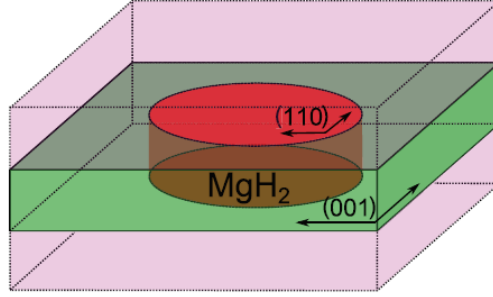
FIGURE 1.4.1. Representation of the Magnesium hydride (in red) surrounded by pure Magnesium (in green). On top and on bottom of the Mg layer are two other layers, in pink [15].

p_{eq}^{nano} of a thin film [15]:

$$ln\left(\frac{p_{H_2}^{nano}}{p_0}\right) = \frac{1}{RT}\left(\Delta_f G^0_{MgH_2} + \sum_i (A\gamma)_{MgH_2|i} - (A\gamma)_{Mg|i}\right) \tag{1.4.4}$$

where A is the interface area per unit mole and i indicates the different interfaces in the sample (for an example see Figure 1.4.1). Comparing Eq. 1.4.3 and Eq. 1.4.4 we can study the equilibrium pressure for a thin film compared to the bulk:

$$ln\left(\frac{p_{H_2}^{nano}}{p_{H_2}^{bulk}}\right) = \frac{1}{RT}\left(\sum_i (A\gamma)_{MgH_2|i} - (A\gamma)_{Mg|i}\right) = \frac{1}{RT}A\Delta\gamma \tag{1.4.5}$$

in the second passage, to simplify the equation, we consider only one type of interface and we assume that the interface area per unit mole A does not vary with hydride formation – this corresponds to ignoring the $MgH_2|Mg$ interface, which is justified by the small area compared to other interfaces. $\Delta\gamma$ represents the interface energy difference between Mg and MgH_2. At this point if we consider a cylindrical shape of the hydride we can write the area as $A = 2V/d$, where d is the thickness of the film and V is the volume per unit mole. We finally obtain:

$$ln\left(\frac{p_{H_2}^{nano}}{p_{H_2}^{bulk}}\right) = \frac{2V\Delta\gamma}{RT}\frac{1}{d} \tag{1.4.6}$$

Therefore if $\Delta\gamma > 0$ – meaning that the hydride has a higher interface energy than the metal – we expect the equilibrium pressure to increase as we consider thinner films. This behaviour was experimentally observed for the first time by Mooij et al. as is shown in Figure 1.4.2. In the case in which $\Delta\gamma$ were negative the equilibrium pressure of the thin film would decrease with respect to the bulk, thus stabilizing the system.

1.4.2. Effects on the solubility limit. As introduced in the previous paragraph the solubility limit indicates the maximum hydrogen concentration at which we still have the solid solution or α-phase. In the first chapter it was stated that hydrogen atoms occupy interstitial sites in the metal's crystal lattice; that is only partially true as there are other sites that can be occupied, namely: surface, subsurface, grain boundaries, dislocations and vacancies (see Figure 1.4.3). The presence of lattice defects and the
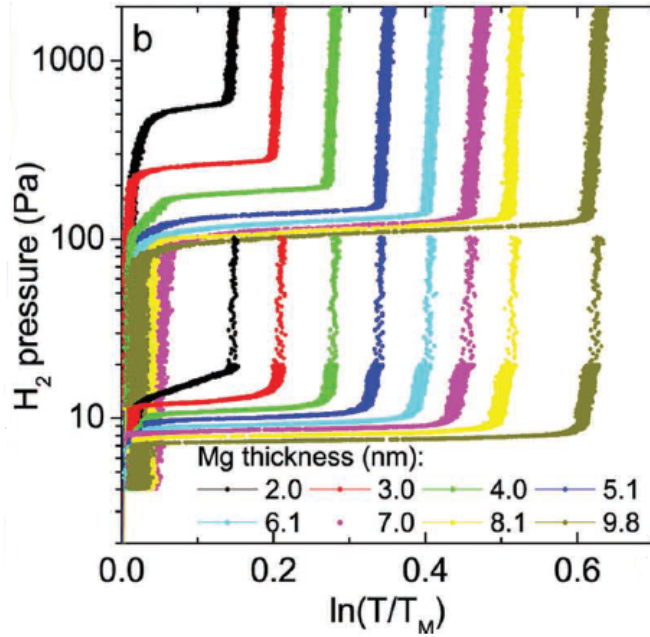
FIGURE 1.4.2. Pressure-concentration isotherms for Mg thin films of different thickness. We can see the pressure plateau increase as the thickness decreases. The concentration is measured indirectly from the film's relative transmittance [15].
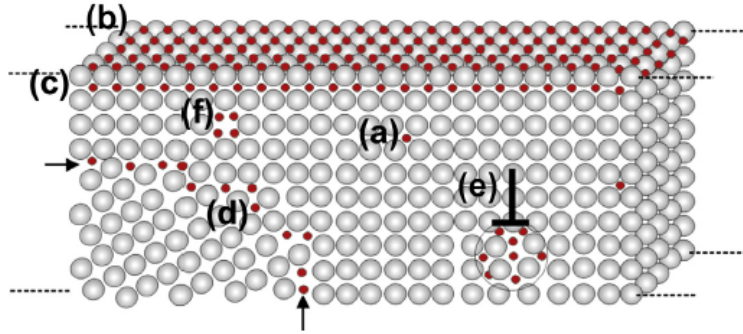

FIGURE 1.4.3. Hydrogen sites in a metal lattice: (a) interstitial sites, (b) surface sites, (c) subsurface sites, (d) grain boundaries, (e) dislocations and (f) vacancies [6].

surface sites can affect the hydrogen solubility in a metal. This effect is particularly relevant in a thin film due to the larger volume fraction of defects and surface to volume ratio. The solubility limit variation due to surface sites in a film of thickness d is given by [6]:

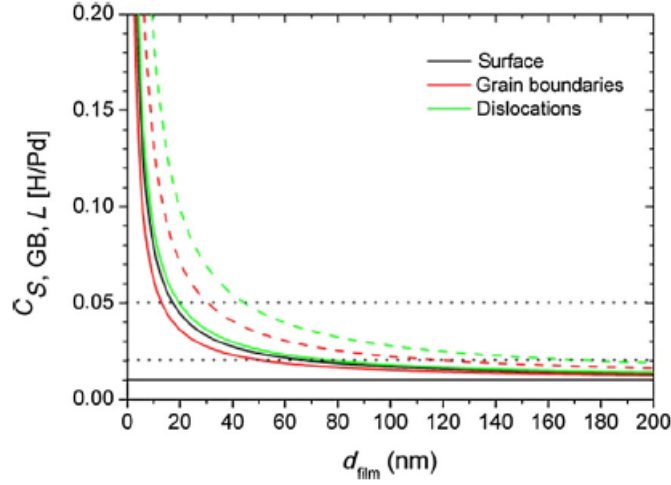$$c_{\alpha,S} = \frac{d - d_{surf}}{d}c_0 + \frac{d_{surf}}{d}c_s \tag{1.4.7}$$

FIGURE 1.4.4. Solubility limit of hydrogen in the α-phase as a function of the film thickness considering the contribution of surface sites (black line), grain boundaries sites with $d_{grain} = d_{film}$ (red line) and misfit dislocations with 10nm distance (green line). The red dashed line combines the effect of surface and misfit dislocations, while the red dashed line combines surface and grain boundaries [6].

where d_{surf} is the surface and subsurface thickness (for example $0.7nm$ for Pd) and c_s is the surface hydrogen concentration (for example $1H/Pd$ for Pd), while c_0 is the bulk solubility limit. The contribution from grain boundaries is given by [6]:

$$c_{\alpha,GB} = \frac{d - d_{GB}}{d^2}c_0 + \frac{2d_{GB}d}{d^2}c_{GB} \qquad (1.4.8)$$

assuming spherical grain boundaries of thickness d_{GB} and with solubility c_{GB}; in the case of PdH we have $d_{GB} = 0.9nm$ and $c_{GB} = 0.3H/Pd$. The solubility limit can also be increased by misfit dislocations that arise at the sample-substrate interface when there is a lattice mismatch. The relation between solubility limit and film thickness is represented if Figure 1.4.4 considering the contribution of surface, grain boundaries, misfit dislocations and their combined effects. As we can see these corrections to the solubility limit are strongly related to the film thickness d, and become less and less relevant as the film grows thicker.

1.4.3. Effects of stress. As described in paragraph 1.2.3, hydrogen absorption deforms the metal's crystal structure and this can contribute to destabilizing the metal-hydrogen system. This deformation introduces stress in the crystal, that can be described with a linear approximation, as long as no defects form. The relationship between the strain tensor ϵ and the stress tensor σ is then given by Hooke's law:

$$\sigma_{ij} = C_{ijkl}\epsilon_{kl} \qquad (1.4.9)$$

where C is the elasticity tensor. The elastic energy density is then:

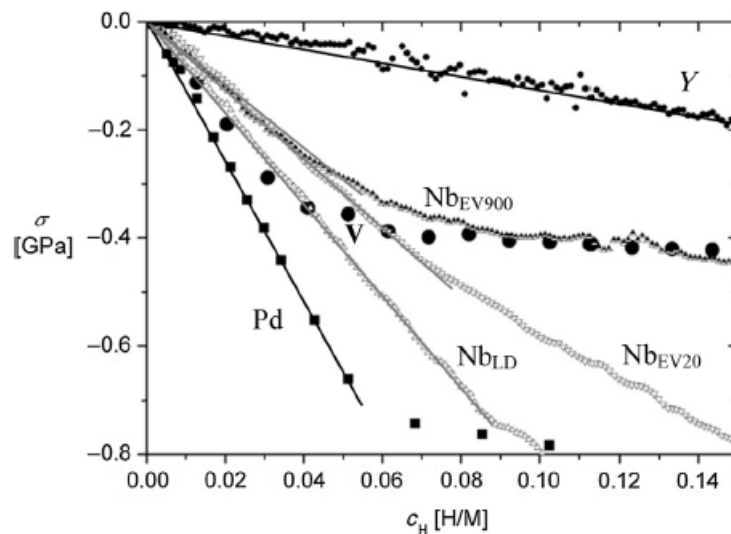$$f = \frac{1}{2}C_{ijkl}\epsilon_{ij}\epsilon_{kl} \qquad (1.4.10)$$

FIGURE 1.4.5. Stress as a function of hydrogen concentration for 200nm Niobium Nb, Yttrium Y and Palladium Pd thin films [6].
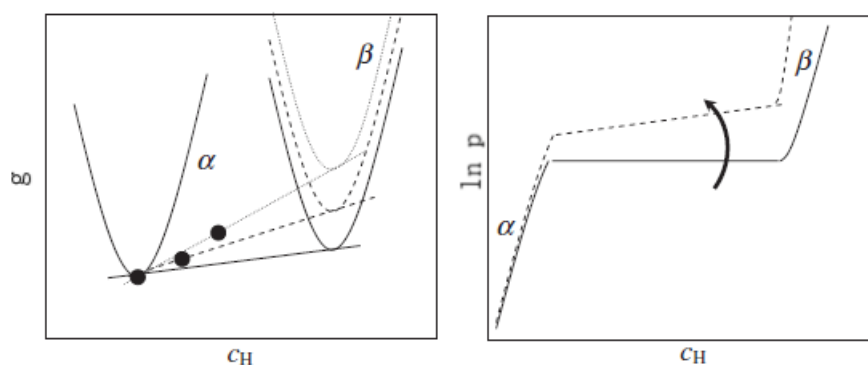

FIGURE 1.4.6. The effect of increased free energy in the β-phase due to elastic energy following hydrogen absorption causes an increase of the free energy with H concentration, manifesting in an inclined pressure plateau [6].

The strain tensor, describing lattice deformation, is at first order proportional to the hydrogen concentration in the metal so, as long as Eq. 1.4.9 holds, we expect the strain to grow linearly with the hydrogen content. This is in fact observed experimentally up to a certain concentration known as yield concentration, as is shown for different metals in Figure 1.4.5. After the yield concentration the stress slope decreases and the linear relation ceases to be valid. This can be explained by stress relaxation mechanisms such as the formation of a dislocation or film detachment.

The effect of stress in thin films also manifests in the pressure-concentration isotherms. As the hydrogen content increases so does the free energy of the system, due to the increased elastic energy. As is shown if Figure 1.4.6 this causes an increase in the chemical potential with hydrogen concentration, which can be observed as a pressure plateau inclined upwards.

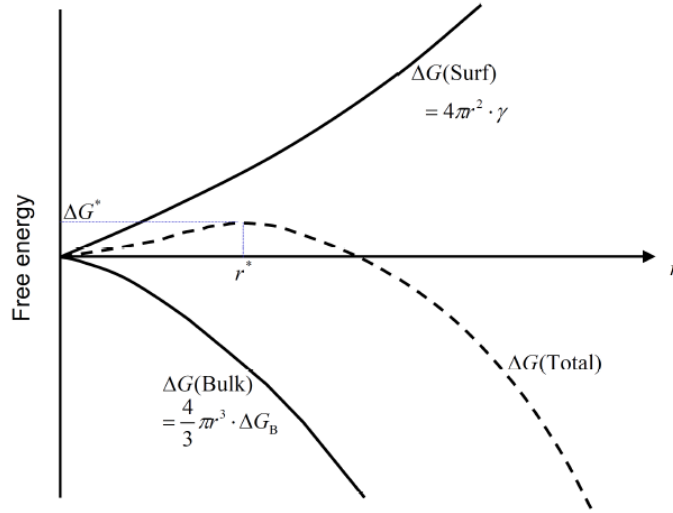## 1.5. Nucleation and growth of the hydride phase

FIGURE 1.5.1. Variation of the free energy upon creation of a nucleus of radius r of β-phase in the α-phase matrix [16].

The creation and growth of the hydride phase in the α-phase matrix can be described by classical nucleation theory [17]. As outlined in previous paragraphs the free energy variation upon nucleation accounts for the free energy difference between hydride and solid solution, but it also contains terms related to interface energy and elastic energy. In particular if we disregard the elastic term and consider a spherical hydride of radius r the free energy variation upon hydride formation ΔG will be:

$$\Delta G = \frac{4}{3}\pi r^3 \Delta G_B + 4\pi r^2 \gamma \qquad (1.5.1)$$

where ΔG_B is the bulk term related to the difference in free energy between the two phases and γ is the interface energy between α and β phase.

Figure 1.5.1 represents the interplay between these two terms. Due to the positive interface energy, the creation and growth of an hydride nucleus increases the total free energy up to the critycal radius r^*. After this value an increase in the nucleus size will lower the free energy; the critical radius therefore marks the smallest dimension of a stable nucleus. Its value is given by [16]:

$$r^* = -\frac{2\gamma}{\Delta G_B} = \frac{2\gamma}{\Delta(\mu_{load} - \mu_\beta)\Delta c} \qquad (1.5.2)$$
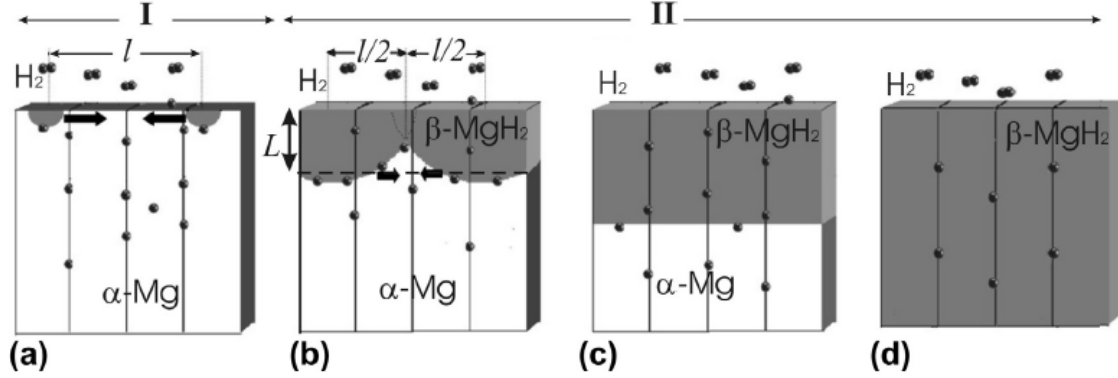
FIGURE 1.5.2. Model for hydride nucleation and growth [**17**].

in the second passage the driving force for nucleation is written as the difference in chemical potential between the hydrogen atoms during loading and in the β-phase multiplied by the variation of hydrogen concentration. In the case of gas loading μ_{load} is given by Eq. 1.3.1. We notice that the dimension of the critical nucleus is inversely proportional to the driving force: for larger driving forces even smaller nuclei will be stable. The maximum of the free energy, reached at the critical nucleus, is called the nucleation barrier ΔG^* and is also related to the driving force [**16**]:

$$\Delta G^* = \frac{16}{3}\pi \frac{\gamma^3}{\left(\Delta(\mu_{load} - \mu_\beta)\Delta c\right)^2} \tag{1.5.3}$$

The nucleation barrier is finally related to the nucleation rate $\dot{N}$, which is the rate at which new hydride nuclei are formed:

$$\dot{N} \propto exp\left(-\frac{\Delta G^*}{RT}\right) \tag{1.5.4}$$

This means that a large driving force will produce a smaller nucleation barrier and therefore a higher nucleation rate. Putting together all these elements, as the driving force increases we will observe a large number of small hydride nuclei.

The formation of these nuclei does not usually start in the bulk of the material, but it is generally located at the surface. A model for their growth has been proposed by Uchida et al. and is represented in Figure 1.5.2. At first hydride nuclei are created at the surface and grow independently at a mean distance l. As their radius reaches the value $l/2$ a layer of hydride is created at the surface, the mean thickness of this layer is $L = l/2$. From this point on the hydride layer propagates downwards until eventually covering the whole volume. Since the diffusivity of hydrogen is much smaller in the hydride phase compared to the α-phase – $D_H^{MgH_2} \sim 10^{-27} m^2/s$ while $D_H^{Mg} \sim 10^{-10} m^2/s$ – we can identify two regimes: in regime I, before neighbouring hydrides touch, the growth is driven by hydrogen diffusion in the α-phase, while in regime II the growth is driven by diffusion along grain boundaries in the β-phase and at the $\alpha - \beta$ interface.

The hydride layer that characterizes regime II is called the blocking layer because, due to the low hydrogen diffusivity, it slows down the absorption and desorption of hydrogen.
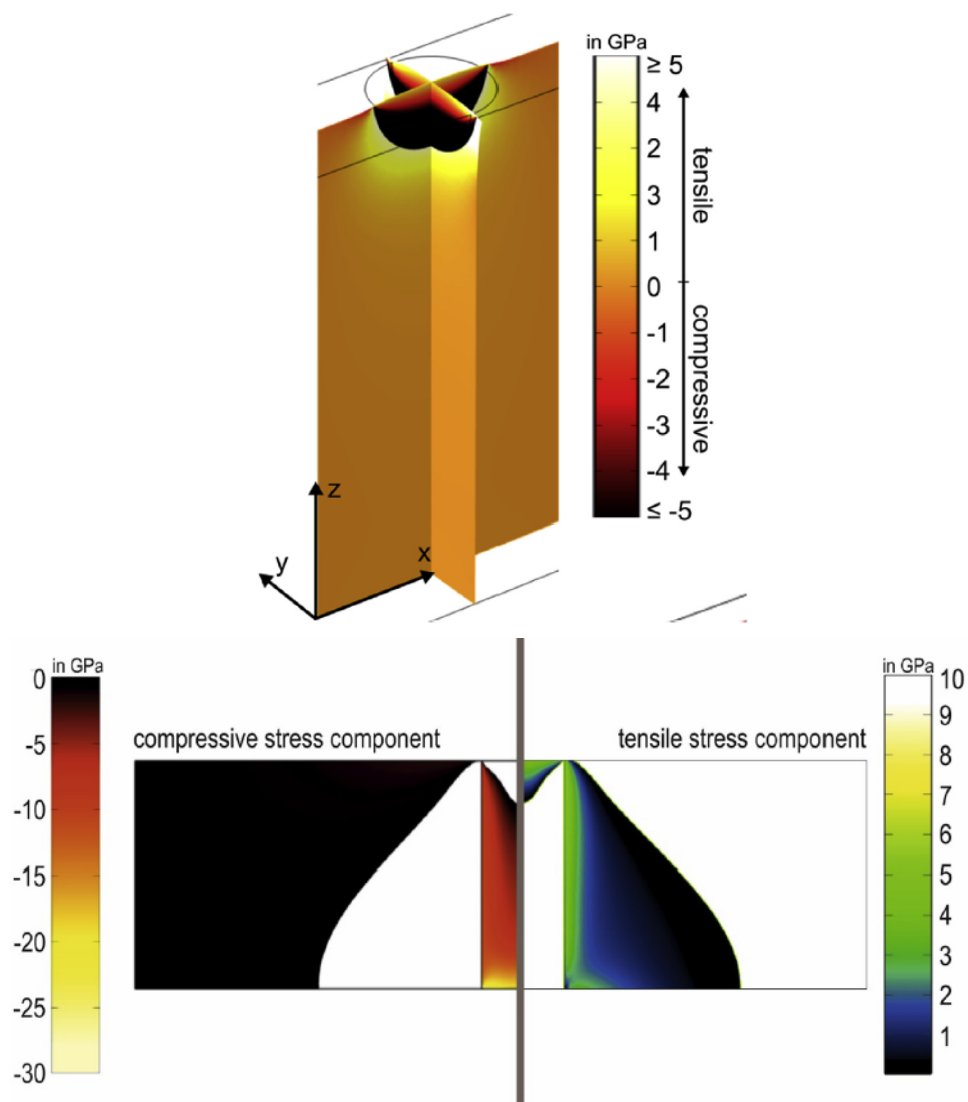
FIGURE 1.5.3. Stress distribution for a sphere and for a cylinder of MgH_2 in a Mg matrix [**18**]. When the hydride has a spherical shape tensile stress develops underneath, favouring a growth in this direction. When the hydride is cylindrical we have compressive stress at the bottom and tensile stress on the sides, favouring a half-sphere growth.

The thickness of the blocking layer depends on the applied driving force: a higher driving force will produce small nuclei closer to each other and so a thinner blocking layer while a lower driving force will produce a larger blocking layer. However, a low driving force will extend the duration of regime I since the nuclei will be further apart and take more time to touch each other, that's why lower driving forces counterintuitively lead to faster absorption and desorption kinetics.

The growth of the hydride can partially be explained with thermodynamic considerations involving stress and elastic energy. As is explained in the work of Hamm et al.,

tensile stress arises below the initial hydride nucleus (see Figure 1.5.3), which will lower the local hydrogen chemical potential thus creating a region for preferred hydride growth. This causes the hydride to grow at first into a cylinder. In this cylinder shape compressive stress arises at the bottom (Figure 1.5.3), increasing the chemical potential, while tensile stress is present at the sides of the cylinder; this situation encourages the growth in a half-sphere shape, in agreement with the previously presented model. However, lateral growth of fingers from the cylinder or half-sphere shape can also be observed [18]. This cannot be explained by thermodynamics arguments since the compressive stress would discourage growth in this direction, but can be understood considering the very low diffusivity of hydrogen in magnesium hydride – which is at maximum $D_H^{GB} \sim 10^{-17} m^2/s$ along grain boundaries – compared to hydrogen in the α-phase. This can lead to lateral growth of the hydride because of higher hydrogen availability with respect to the bottom of the hydride, where hydrogen can arrive only through grain boundaries.

1.6. Mg-Pd and Mg-Ti phase diagrams

Figure 1.6.1 shows the phase diagrams of the Mg-Pd and on the Mg-Ti systems. The Mg-Ti systems is characterized by a very low mutual solubility of the two elements, and by the presence of no intermetallic compounds. The solid phases are just given by the equilibrium of the magnesium solid solution (Mg) and α or β pure Ti, depending on the temperature. On the contrary, the Mg-Pd systems exhibits a richer phase diagram with a large number of intermediate phases between (Mg) and (Pd) solid solutions. More details on the equilibrium phases, such as the composition and space group, are reported in Table 1.6.1. We can also notice that the Mg solubility in Pd is larger than the Pd solubility in Mg.

TABLE 1.6.1. Pd concentration and space group of the equilibrium phases of the Mg-Pd system [20].

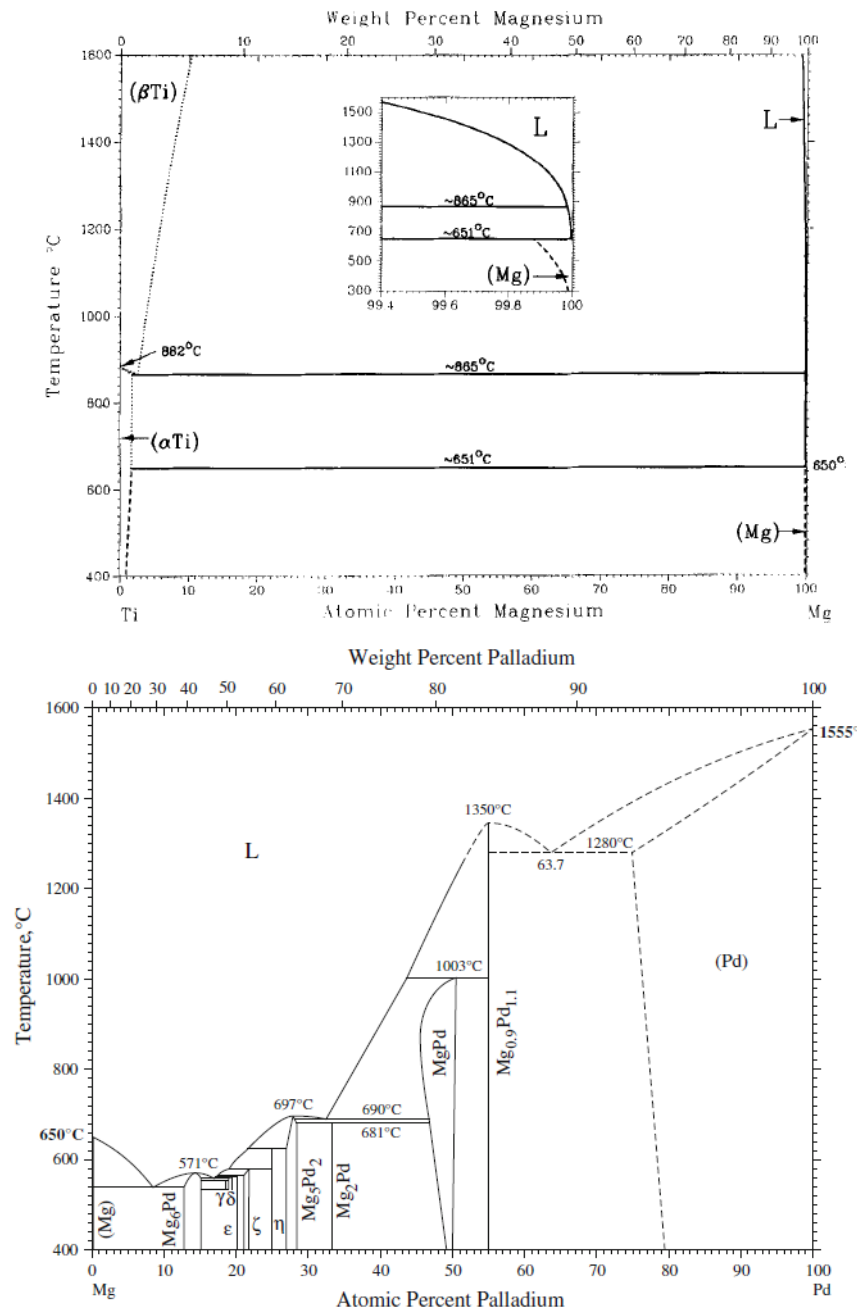| Phase	Composition (Pd at.%)	Space group
(Mg)	0	$P6_3/mmc$
Mg_6Pd	12.7-15.2	$Fm\bar{3}m$
$\gamma(Mg_{57}Pd_{13})$	18.6	
$\delta(Mg_{56.4}Pd13.5)$	19-19.5	
$\epsilon(Mg_{306}Pd_{77})$	20.1	
$\zeta(Mg_{78.5}Pd_{21.5})$	21-21.8	
Mg_3Pd	25	$P6_3/mmc$
Mg_5Pd_2	27-28.4	$P6_3/mmc$
Mg_2Pd	33.3	
$MgPd$	45.5-50	$Pm\bar{3}m$
$Mg_{0.9}Pd_{1.1}$	55	$P4/mmm$
(Pd)	75-100	$Fm\bar{3}m$

FIGURE 1.6.1. Phase diagrams of the Mg-Ti [19] and of the Mg-Pd [20] systems .

2. Experimental Methods

Four different types of samples were deposited to study the behaviour of Hydrogen in Magnesium thin films. Information on the behaviour of the system was collected by measuring the isotherm curves. To do so controlled loading of hydrogen in the thin films is necessary, this was achieved using two different techniques: electrochemical loading in KOH and loading from the gas phase.

2.1. Sample preparation

2.1.1. Cathode beam sputtering. All the samples were prepared by cathode beam sputtering. This technique belongs to the family of Physical Vapour Deposition, meaning that the deposited material is transported from the source to the substrate in the vapour phase. In cathode beam sputtering, the material is ejected from the source by bombardment with accelerated positive ions of Argon gas (Ar^+); this phenomenon is known as sputtering and gives the name to the whole deposition technique. The whole system must be kept under Ulta-High-Vacuum conditions to make the deposition possible. The Ar^+ ions are created by letting Ar in a magnetic field, that ionizes and confines the gas creating a plasma. The ions are then accelerated towards the targets by two grids at different voltages.

The argon-ion beam sputter source was implemented in an ultra-high vacuum apparatus with a background pressure lower than $10^{-9}mbar$. This low pressure is necessary to sputter pure Magnesium. A prechamber allowed to insert the substrates and to remove the prepared samples without breaking the UHV condition. The background pressure of the prechamber was always in the range of $10^{-7}mbar$ before substrates or samples were transferred. The argon pressure during sputtering was around $1.3 \times 10^{-4}mbar$.

Up to four targets could be mounted on a rotating holder, allowing sputtering of different materials without removing the sample or the target. For this work three targets were used: Magnesium, Palladium and Titanium. Mg and Ti targets had to be cleaned before deposition by pre-sputtering for a few hours to eliminate surface oxides (see Table 2.1.1). The deposition rates for the three different targets were determined by sputtering on a substrate for a set amount of time and then measuring the thickness of the sample by X-Rays Reflection (XRR) and are also reported in Table 2.1.1. All samples were deposited at room temperature.

2.1.2. Examined samples. Four different types of samples were prepared to study the behaviour of the Mg-H system, schematically represented in Figure 2.1.1. All samples were deposited on $1cm \times 1cm$ Sapphire (1000) substrates, the substrates were polished on both sides to allow optical measurements. Table 2.1.2 summarizes the deposition times and nominal thickness for each layer of the created samples. The first three types of samples (Figure 2.1.1 A-C) were used to study the behaviour of Magnesium during hydride formation for different thicknesses of the film, and contain one layer of Magnesium covered by one layer of Palladium. The Pd layer was necessary to protect Magnesium

TABLE 2.1.1. Deposition rate and required pre-sputter time for the used targets.

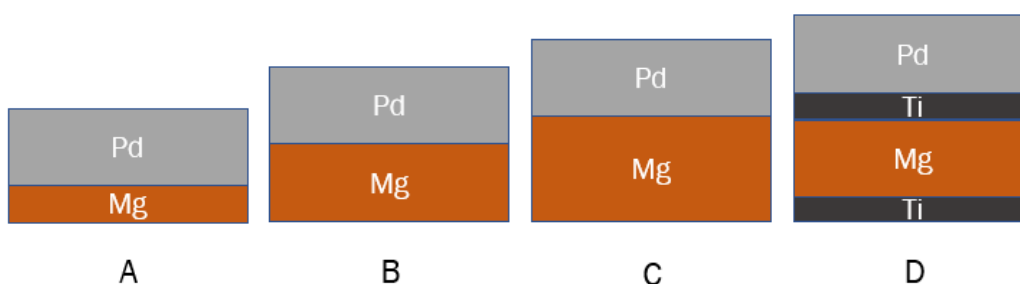| Target	Deposition rate (nm/min)	pre-sputter time
Mg	1.3	3h
Pd	2.13	-
Ti	1.19	2h

FIGURE 2.1.1. Schematic drawing of the prepared and analyzed samples.

TABLE 2.1.2. Deposition time and nominal thickness of the layers of the samples represented in Figure 2.1.1. The nominal thickness is obtained from the deposition rates reported in Table 2.1.1.

Sample	Material	Deposition time	Nominal thickness
A	Mg	10 min	13 nm
	Pd	15 min	32 nm
B	Mg	20 min	26 nm
	Pd	15 min	32 nm
C	Mg	30 min	39 nm
	Pd	15 min	32 nm
D	Mg	20 min	26 nm
	Ti	8 min 30s	10 nm
	Pd	15 min	32 nm

from oxidation and also to accelerate the process of hydrogen absorption. The thickness of this Pd layer was held constant for all the deposited samples, for an easier comparison of the results. Some samples were also prepared by surrounding the Mg layer with two thinner layers of Titanium (Figure 2.1.1 D) to prevent alloying with the Pd layer; this allows us to determine whether alloying affects the behaviour of the system during hydrogen absorption.

2.2. Electrochemical loading

Electrochemical loading introduces hydrogen in a sample using electrochemical reactions at the sample's surface. Usually, an electrochemical cell in the three-electrodes geometry is employed. The sample is the cell's working electrode, and a counter electrode is used to generate pulses of current inside the cell. If a suitable electrolyte is chosen hydrogen will then be absorbed by the sample to allow current propagation. The variation in hydrogen concentration Δc_H following a current pulse can in principle be found using Faraday's law [6]:

$$\Delta c_H = \frac{I\Delta t}{F}\frac{1}{n_{Me}} \tag{2.2.1}$$

where I is the current's intensity, Δt is the pulse's duration, F is Faraday's constant giving the charge of a mole of electrons and n_{Me} is the number of moles of metal, which can be found dividing the metal's total volume by its molar volume. In fact, $I\Delta t$ gives the total charge entering the sample, which is transformed in moles of hydrogen dividing by Faraday's constant. At the same time, the reference electrode is measuring the potential (or electromotive force) inside the cell. When an equilibrium condition is reached, after the current pulse, this quantity corresponds to Nernst potential U and it is therefore related to the hydrogen chemical potential by Nernst equation [6]:

$$\mu_H = -(U - U_0)F \tag{2.2.2}$$

where the reference voltage U_0 depends on the chosen reference electrode and electrolyte. Otherwise, the measured equilibrium potential can also be translated to an equivalent hydrogen pressure:

$$U - U_0 = -\frac{RT}{2F}ln\left(\frac{p_{H_2}}{p_0}\right) \tag{2.2.3}$$

Acquiring pressure-concentration isotherms is therefore relatively easy. The concentration axis can be found directly from equation 2.2.1, while a quantity equivalent to the pressure can be obtained simply by measuring the electromotive force once the system has reached an equilibrium condition after the current pulse.

2.2.1. Experimental Setup for electrochemical loading. Figure 2.2.1 represents the circuit used to load and unload hydrogen in the sample. The current through the counter electrode (CE) was generated using a DC voltage source, and its value was measured through the voltage drop across a 100Ω resistor. A timer was set in series to the resistor to control the duration of the current pulse and finally connected to the CE. The other terminal of the voltage source was connected to the sample or working electrode (WE). The voltage between the sample and the reference electrode (RE) was measured with a DAQ board, to which an impedance converter was added to prevent current leakage. The voltage drop across the resistance was also acquired using a second channel of the DAQ board. This part of the setup allowed to measure the Nernst potential and the current entering the sample, from which the concentration can be derived according to equation 2.2.1. An optical method to indirectly measure hydrogen concentration was also employed. During hydride formation Mg and Pd become more transparent; hydrogen concentration can therefore be measured indirectly by recording variations in the film's transmittance. In particular, according to Lambert-Beer's law,
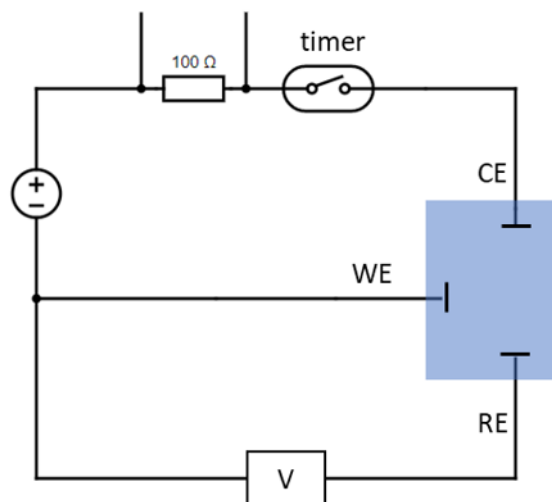
FIGURE 2.2.1. Schematic drawing of the circuit for hydrogen loading.

TABLE 2.2.1. Technical information on the elements used for electrochemical loading of hydrogen.

Voltage source	Knick Präzisions Spannungsgeber s13
	Keithley 2601 SYSTEM Source Meter
Resistor	DEKADE Typ 4205
DAQ	IOtech Personal Daq/56
DAQ software	Personal DAQ View Plus
Microscope	Leica DM 2700 M
Objective	10x 0.25 HI PLAN
Camera	Leica MC170 HD
Camera software	LAS V4.9

the hydrogen concentration is proportional to the logarithm of the relative variation of the film's transmittance T [21]:

$$c_H \propto ln\left(\frac{T}{T_M}\right) \tag{2.2.4}$$

where T_M is the initial transmittance of the film. The transmittance is measured using an optical microscope with a light source below the sample and the objective connected to a CCD camera above it. The optical part of the setup is represented in Figure 2.2.2. Technical information on the employed instruments and software are reported in Table 2.2.1. As can be seen in Table 2.2.1, the voltage source had to be replaced due to damage.

All operations for loading and unloading had to be performed under a fume hood to prevent hazard from the used electrolyte. The electrochemical cell is represented in Figure 2.2.3. We can see the RE which was based on mercury oxide (Hg/HgO), the platinum counter electrode and the sample. To make sure that the sample was in contact
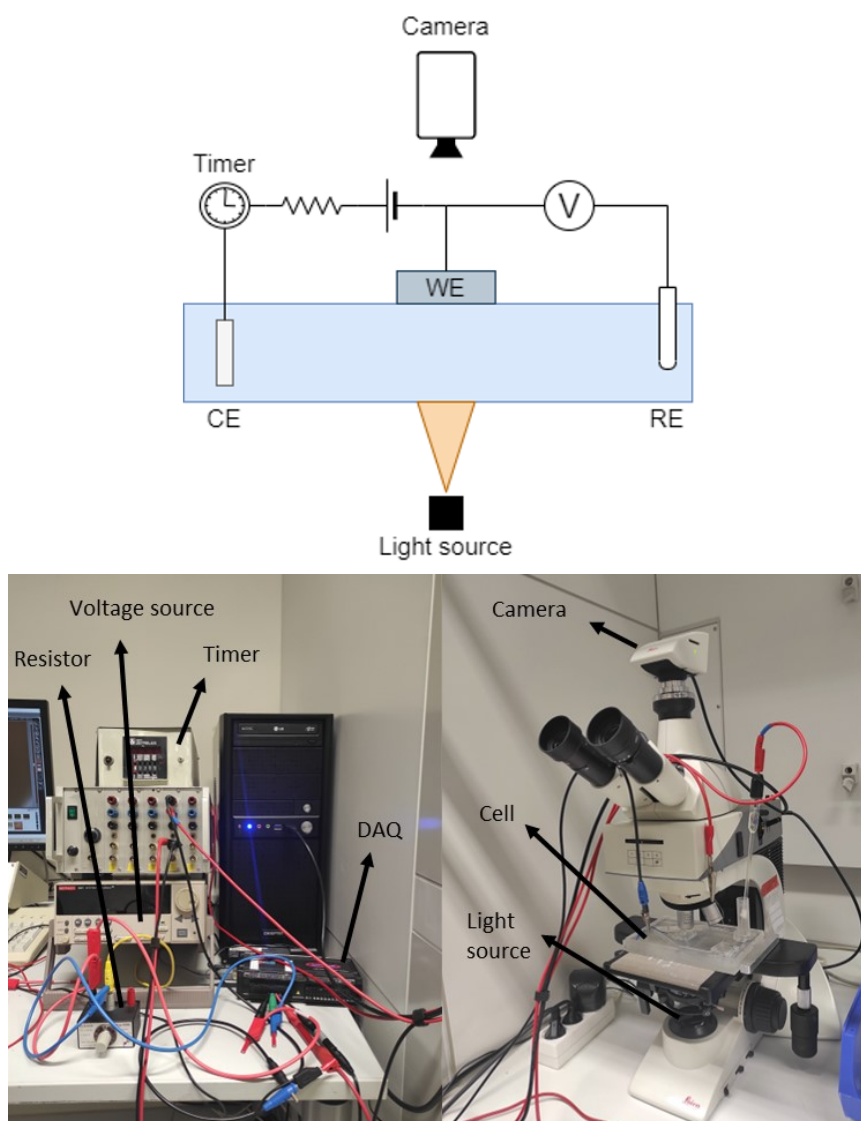
FIGURE 2.2.2. Schematic drawing and pictures of the complete setup for electrochemical hydrogen loading, including the elements needed for optical measurements.

with the electrolyte only through the Pd-coated surface and not from the sides it was pressed onto a rubber ring by a plastic mask, secured with four screws. This sealing is extremely important because leakage of the electrolyte leads to self-loading of the film, which increases the potential above the Mg hydride formation plateau therefore making it impossible to acquire the isotherms. At the same time the applied pressure can't be too large to avoid cracking or otherwise damaging the substrate. The film is connected to the voltage source using a small copper wire which touches the conductive surface of the sample in one of its corners, outside of the rubber ring. To prevent KOH leakage the electrochemical cell was slightly modified reducing the diameter of the rubber ring from 9
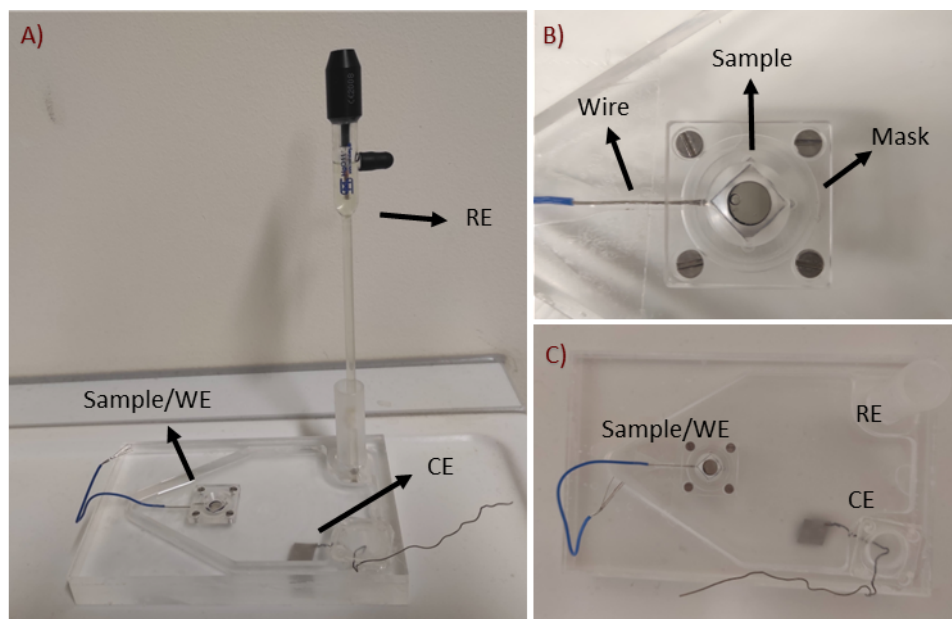
FIGURE 2.2.3. Electrochemical cell used for hydrogen loading in 5M KOH: A) complete view of the cell with installed sample, reference electrode (RE) and counter electrode (CE). B) closeup view of the sample covered by a plastic mask to ensure that no electrolyte leaks out of the cell. The blue wire touches the sample on one of its corners and is used to connect it to the voltage source. C) Top view of the cell without the reference electrode.

to 8 mm, therefore leaving more space for the wire to touch the sample's surface without risking to overlap with the rubber ring, which would make the sealing ineffective. This second version of the cell also contained a smaller volume of electrolyte to reduce cell resistance effects. The mask has a circular hole to allow optical measurements.

2.2.2. KOH as an electrolyte. The electrolyte used in the electrochemical cell was 5M potassium hydroxide (KOH). When in contact with water the KOH molecule splits in two ions, K^+ and OH^-, which allow electricity conduction. However, the process used to load hydrogen inside the samples differs from the general procedure that was introduced in the previous paragraph, because the electrolyte is not directly employed in loading and unloading processes, but hydrogen is produced by water electrolysis. The electrochemical reactions happening at the sample's surface during loading and unloading are represented in Figure 2.2.4. For hydrogen loading a negative voltage has to be applied to the sample. This will start the water reduction reaction:

$$H_2O + e^- \longrightarrow OH^- + H_{ads} \tag{2.2.5}$$

the produced hydrogen atoms can be adsorbed at the sample's surface and then diffuse inside the sample to eventually create the hydride phase. For the opposite process of hydrogen desorption a positive voltage has to be applied, leading to the inverse reaction:
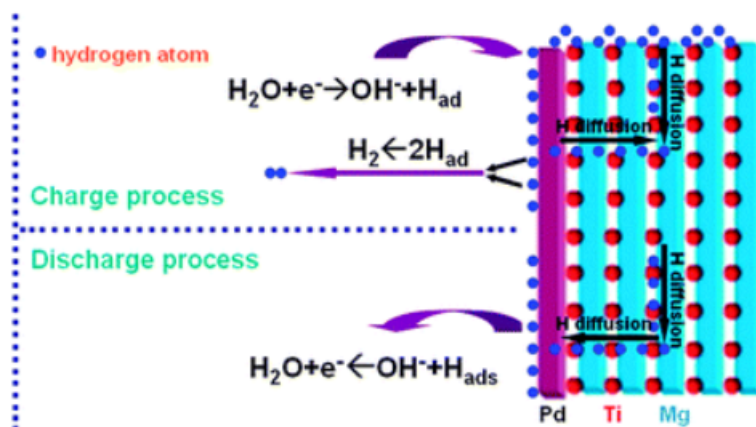
$$OH^- + H_{ads} \longrightarrow H_2O + e^- \tag{2.2.6}$$

FIGURE 2.2.4. Representation of the electrochemical reactions at the sample's surface during hydrogen loading and unloading in KOH [**22**].

Only looking at these reactions one might think that hydrogen loading and unloading could be performed with only water in the electrochemical cell; in practice that is not possible because it would cause oxidation in the sample's surface which would make hydrogen absorption impossible and cause damage to the film. Hence, KOH is applied to prevent sample oxidation. Cyclic voltammetry measurements allowed for a better understanding of the loading and unloading processes and inspired the experimental setup in Figure 2.2.1, which had previously been designed with a current source instead of the voltage generator to control the current intensity. However, by directly controlling the applied voltage we can minimize the blocking layer effect because we can generate just the driving force necessary to start the loading reactions. Before hydrogen loading the cell was also bubbled with Argon gas for 30 minutes, to eliminate oxygen content and therefore avoid oxidation at the surface.

2.2.3. Data Analysis. To obtain the isotherm curves three quantities had to be extracted from the acquired data: a direct measurement of the concentration from equation 2.2.1, an indirect measurement of the concentration from the film images and the value of Nernst potential from the voltages measured with the reference electrode.

(1) **Direct measurement of the concentration**. To obtain the concentration we need the amount of charge entering the sample. This was extracted from the voltage drop across the resistor in series with the voltage generator (see Figure 2.2.1). This quantity was acquired by one of the DAQ channels and integrated over time for each pulse. The obtained value was then divided by 100Ω to have a charge value and then inserted in equation 2.2.1.

(2) **Indirect measurement of the concentration**. This method involved evaluating the film's transmittance, which is proportional to the brightness of the film's image when using an optical microscope with a light source from below. An example of the acquired images is reported in Figure 2.2.5. These images were analyzed with the software ImageJ to obtain the distribution of the pixels' intensity. This distribution was then fitted with a gaussian curve to find the central value. Finally, to evaluate the relative brightness variation, the mean
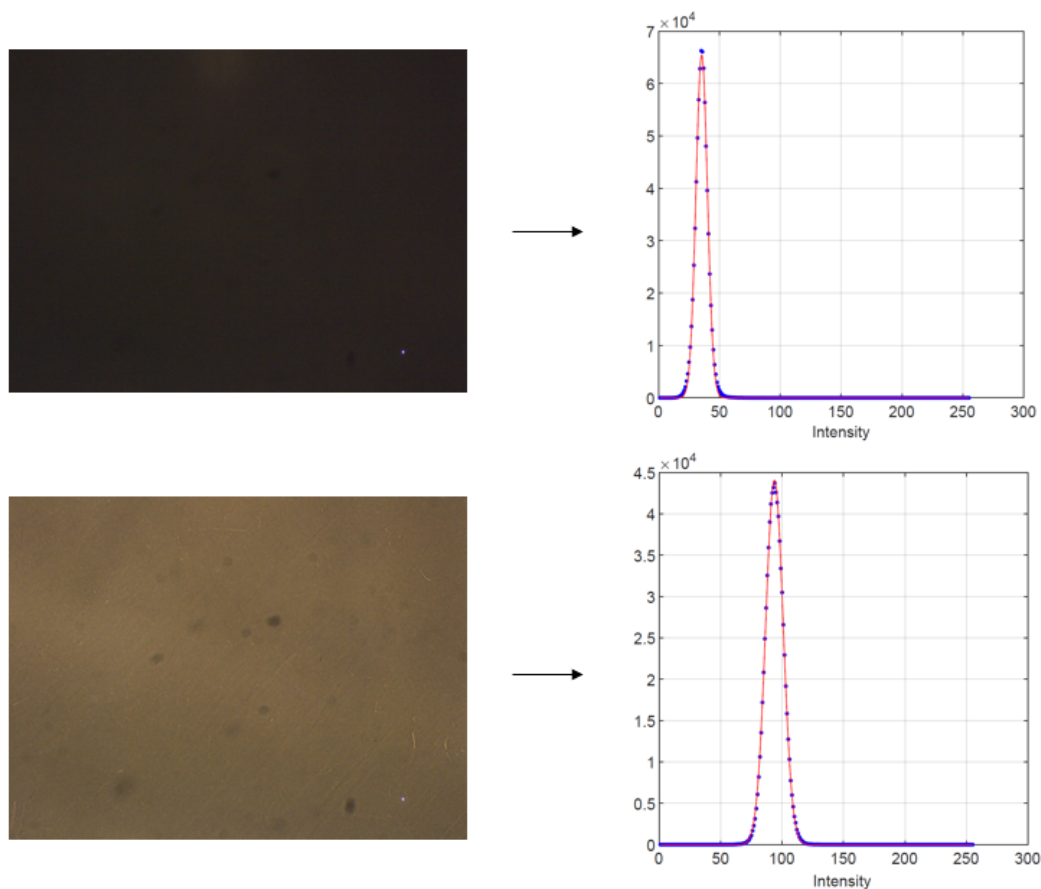
FIGURE 2.2.5. Example of two pictures acquired with the optical microscope and analyzed to find the mean intensity. From each image the intensity distribution was analyzed with ImageJ (the blue dots represent the pixels count for each intensity) and then fitted with a gaussian curve (red line) to obtain the central value.

intensity of the images acquired after every loading step was divided by the intensity of an image acquired before applying any currents to the sample.

(3) **Equilibrium potential**. An example of the voltage registered by the reference electrode during loading is reported in Figure 2.2.6. The shape of the curve will be commented in detail in the following chapter; however, the initial peak corresponds to the current pulse (when the timer is allowing the current to reach the counter electrode). After this, the voltage rapidly decreases and, after a first plateau, it reaches a stable value. To decide which voltage should be plotted in the isotherms as the equilibrium value one technique could consist in always waiting the same time interval after each current pulse, and to take the voltage at that time as the equilibrium voltage. However, since the time needed to reach a stable value is not constant during Mg hydride formation, this leads to plateaus that are quite scattered around a central value. A more reliable method consisted in calculating the derivative of the electromotive force (EMF)
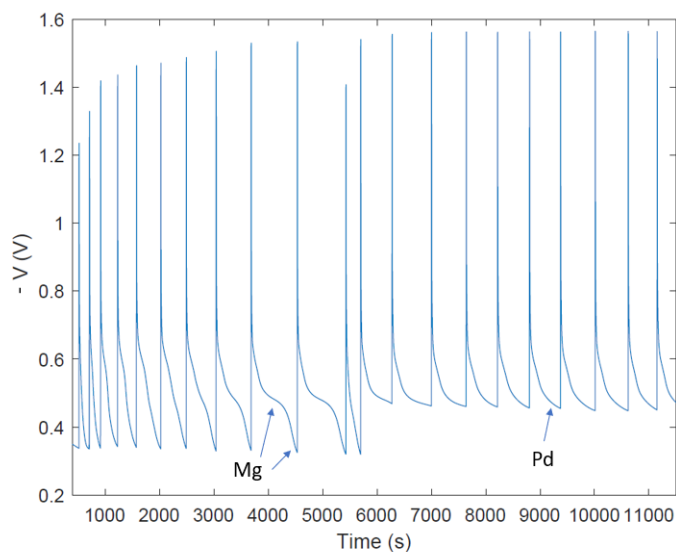
FIGURE 2.2.6. Time evolution of the voltage measured by the reference electrode during hydrogen loading. On the left the double-plateau curves are related to Magnesium hydride formation while the single-plateau curves are related to palladium hydride formation (see arrows). The real value of the voltage would be negative in agreement with the cyclic voltammetry results (Figure 3.1.1), here and in all following Figures the inverse of the voltage is shown for an easier visualization of the plots.

and selecting, after each pulse, points where the derivative has the same value. This can be applied because all curves exhibit a similar shape with two plateaus during Magnesium hydride formation. During palladium hydride formation the curves only have one plateau and the time needed to reach a similar derivative is approximately constant, so this correction becomes unnecessary.

2.3. Gas-phase loading

Hydrogen loading from the gas phase consists in increasing the hydrogen pressure surrounding the sample in controlled steps. After each step we must wait until the sample reaches an equilibrium condition after absorbing part of the hydrogen; the pressure at equilibrium is proportional to the hydrogen's chemical potential according to equation 1.3.1. In the case of bulk samples the pressure variation after hydrogen absorption can be measured if the volume of hydrogen is not too large compared to the sample's volume; this is not the case for thin films due to their very small volume.

2.3.1. Experimental setup for gas-phase loading. The experimental setup consisted in a ultra-high vacuum system that allowed to precisely control the hydrogen pressure applied to the sample, represented in Figure 2.3.1. The sample was placed in a glass tube that could be removed from the rest of the system to install the sample, and then attached again through a CF40 flange secured with six screws. The tube was connected
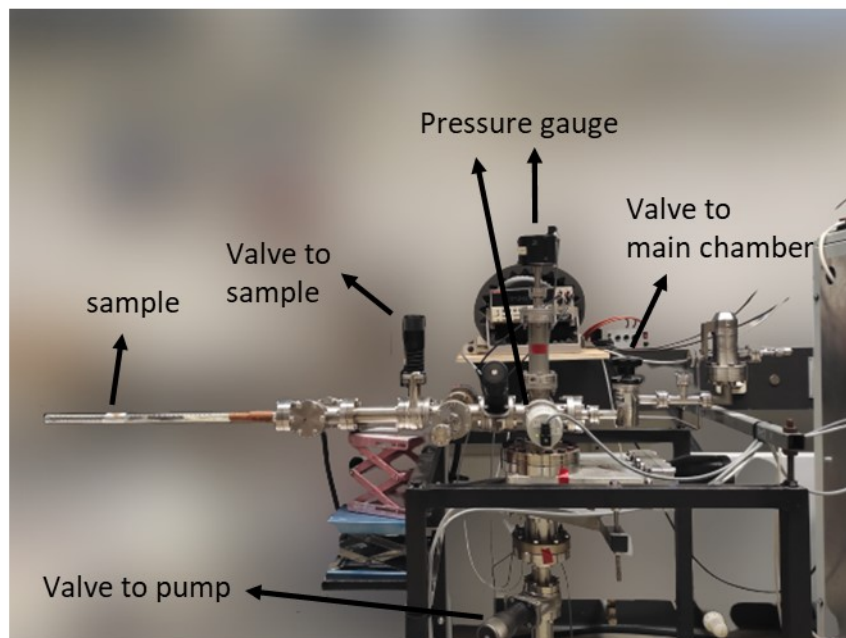
FIGURE 2.3.1. Picture of the experimental setup for hydrogen gas loading.

to the main chamber with a valve that could be kept open or closed. At the bottom, the main chamber was also connected to a turbo molecular pump and to a rotary vane pump to create the initial vacuum condition and to correct the applied hydrogen pressure at every step. The hydrogen gas was coming in through pipes and a flow regulator. An additional valve allowed to completely interrupt the flux of hydrogen.

Before starting any hydrogen loading, a vacuum of at least $2 \times 10^{-7} mbar$ was achieved opening the valves between the sample and the main chamber and between the main chamber and the pump. After that, those valves were closed and the desired pressure was achieved by allowing hydrogen inside the main chamber. Finally, hydrogen was let in the sample's glass tube by opening the valve between the sample and the main chamber; this procedure was repeated for each loading step. The pressure in the system was measured at all times using three vacuum gauges attached to the main chamber with different operative ranges (up to $\sim 1mbar$, from 0.01mbar to 10mbar, and from 1mbar to 1000mbar). All the measured values could be read in the relative displays, the value considered to plot the isotherms was the first one observed after opening the valve to the sample's glass tube.

The hydrogen concentration inside the sample was evaluated with two different indirect methods, based on the metal to insulator transition during hydride formation in Mg. The first method consisted in a four-point measurement of the sample's resistance. To do so four pins touched the sample's surface and were then in contact with four wires leading to a Keithley2000 source measure unit. The measured value was registered every
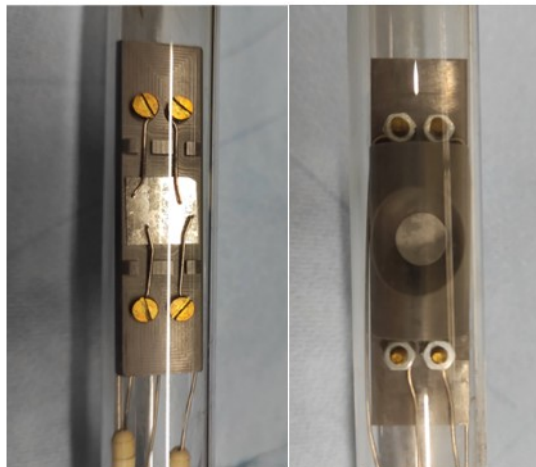
FIGURE 2.3.2. Picture of the sample mounted on its holder for hydrogen gas loading.
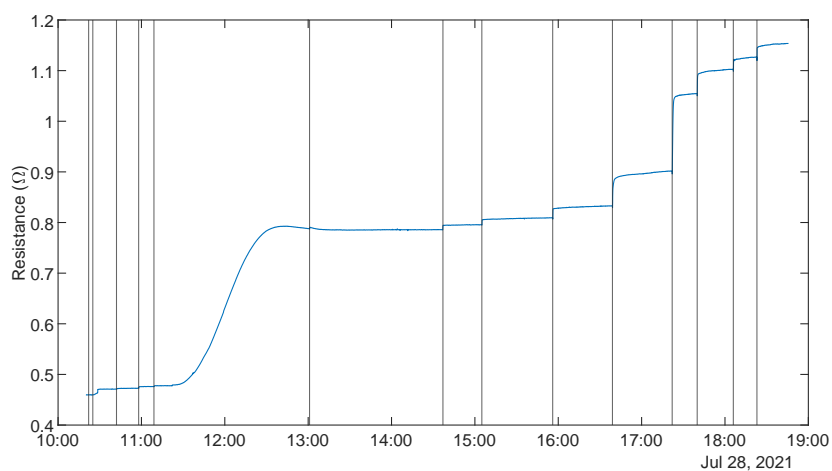

FIGURE 2.3.3. Example of the measured resistance as a function of time during hydrogen gas loading, the vertical lines mark the points at which the hydrogen pressure in the sample's glass tube was increased. After each step the sample was let to reach its equilibrium for a sensible time interval.

second with a computer and a dedicated software. The front and back of the sample holder are represented in Figure 2.3.2. The back of the sample holder has a circular hole to allow for the second method to measure the concentration, which consisted in an evaluation of the film's transmittance similarly to what was done during electrochemical loading. In this case however the setup was more simple because it didn't involve a microscope but just a lamp and a camera attached to a computer to acquire images of the film. This allowed to evaluate the film's brightness but not to choose the magnification.

To construct the pressure-concentration isotherms the applied hydrogen pressure was plotted in logarithmic scale as the y-axis, given its proportionality to the chemical potential. Two different x-axis were constructed. The first one based on the optical measurements, evaluated with the same procedure applied for electrochemical loading (see Figure 2.2.5). The second consisted in the final value of the sample's resistance before applying the following hydrogen pressure, recorded with source measure unit in the four-points measurement setup. An example of the acquired resistance is reported in Figure 2.3.3.

3. Results

This chapter shows the most relevant obtained results. Paragraph 3.1 contains the results for the Cyclic Voltammetry experiments that allowed to better understand the behaviour of KOH as an electrolyte. Paragraph 3.2 reports the isotherm curves for the creation and dissolution of Magnesium hydride. Paragraph 3.3 deals with the different patterns observed during magnesium hydride formation. Paragraphs 3.4 and 3.5 discuss the effect of the magnesium layer's thickness on the plateau EMF and pressure for magnesium hydride formation. Finally, paragraph 3.6 discusses the effect of a Titanium interlayer to prevent Mg-Pd alloying.

3.1. Cyclic Voltammetry

To better understand the behaviour of KOH as an electrolyte Cyclic Voltammetry (CV) measurements were performed on samples of the type B with a potentiostat, while at the same time measuring the film's transmittance with an optical microscope. Cyclic Voltammetry consists in varying the voltage applied through the RE in small steps between two limiting values, and at the same time measuring the current through the CE. The measure can be repeated for a certain number of cycles. The results for CV with in-situ optical microscopy are reported in Figure 3.1.1. The curve is composed of two cycles between 0 and -1.5V, with a step of 20mV/s and the starting point at -0.2V. As we can see, when we start at -0.2V the current is close to zero and it remains so as we move towards more negative potentials; this indicates that no electrochemical reaction is happening at the sample's surface. As the applied potential goes below -1.2V the current moves to negative values; this indicates a reduction reaction which we identify as the one in equation 2.2.5 leading to water electrolysis and hence to hydrogen absorption in the sample. This hypothesis is confirmed by the increase in the brightness of the film's images (images $1 \rightarrow 2$ in Figure 3.1.1), which proves that the hydride is formed. As we move again towards 0V the current decreases and stays close to zero, until a voltage around -0.4V is reached. At this point we see a positive current, that is identified with the reaction in equation 2.2.6 leading to hydrogen desorption from the sample. This is again confirmed by the recorded images that show a decrease in the brightness, meaning that the sample became less transparent and thus part of the hydride was removed (images 3 $\rightarrow 4$ of Figure 3.1.1). The fact that the image does not return to the original brightness can be explained considering that the voltage is changing quickly and that does not allow enough time for the hydrogen to diffuse out of the sample.

While proving that KOH can be used as an electrolyte to load hydrogen in Magnesium thin films, the CV results show already one of the limitations of this electrolyte, which is the high voltage that must be applied to start the reactions leading to hydrogen adsorption. This means that we will have to send current pulses with a high intensity I and, since with the used setup their duration Δt cannot not be shorter than a few seconds to observe some response from the sample, at each loading step a large amount of hydrogen is created. Not all this hydrogen can be absorbed into the sample, but part
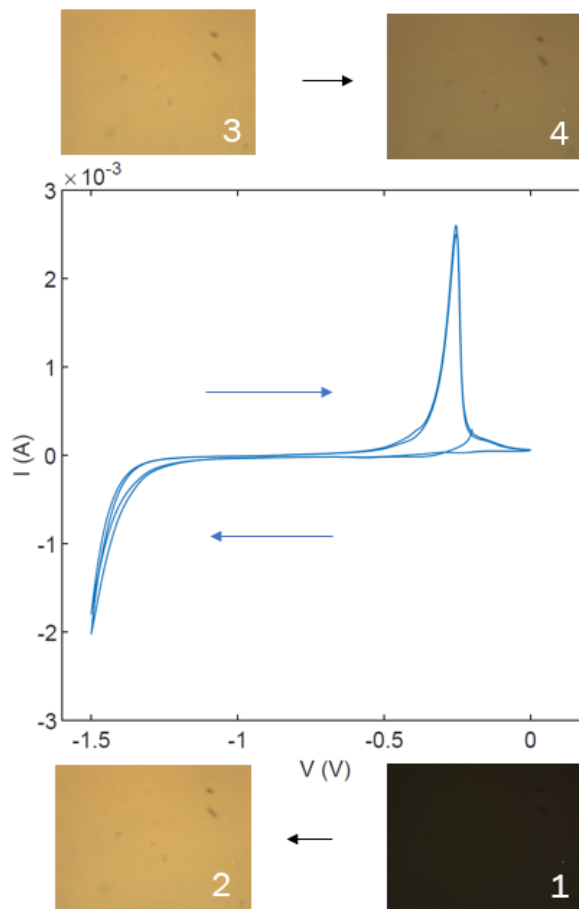
FIGURE 3.1.1. Results of CV measurements on samples of type B using KOH as an electrolyte. Images of the film were acquired during the CV with an optical microsope.
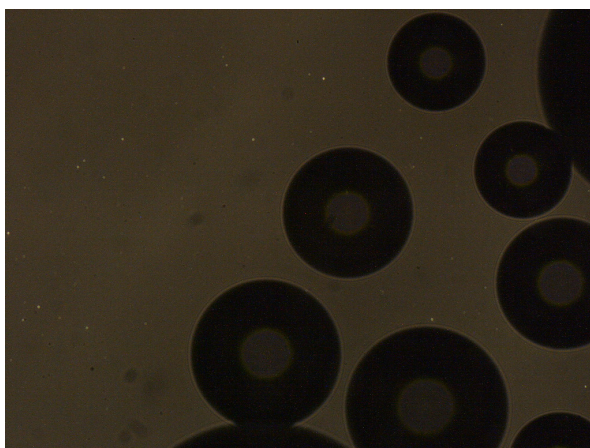

FIGURE 3.1.2. Hydrogen bubbles on the sample's surface during hydrogen loading.

of it creates hydrogen bubbles at the sample's surface, as can be observed in Figure 3.1.2. This makes Faraday's Law (equation 2.2.1) inaccurate when determining the concentration at each loading step because we cannot know how much hydrogen actually entered the sample and how much was eliminated in bubbles; the calculated values will however always be overestimated. Moreover the high driving force is related to a quick formation of the hydride blocking layer in Magnesium, as was discussed in paragraph 1.5. This blocking layer, where the hydrogen diffusivity is significantly lower than in the solid solution, slows down the absorption of hydrogen.

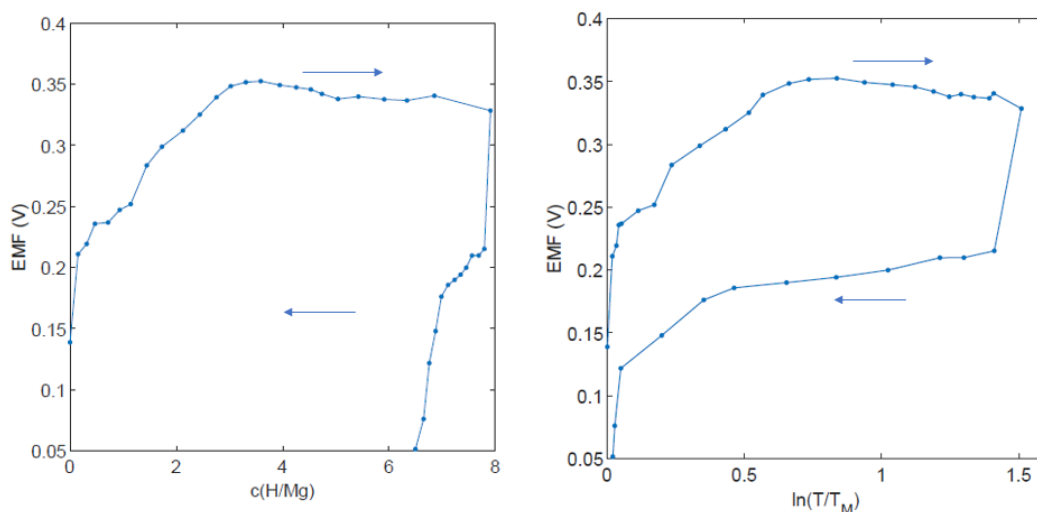## 3.2. Magnesium hydride formation and dissolution isotherms

FIGURE 3.2.1. Isotherms obtained with electrochemical hydrogen loading and unloading in a sample of $\sim 26nm$ Mg and $\sim 32nm$ Pd (Type B in Figure 2.1.1 and in Table 2.1.2). The arrows mark the directions of loading – left to right, in the top part of the curve – and unloading – right to left, in the bottom part of the curve. As expected, the EMF shows two plateaus for magnesium hydride formation and dissolution, separated because of the hysteresis effect. The curve obtained from the transmittance is closed, meaning that the sample returned to its original transparency and hydrogen concentration. This is not mirrored by the isotherm obtained from a direct calculation of the concentration due to hydrogen loss at the sample's surface.

Figure 3.2.1 reports the isotherm curves for a sample of ∼26nm Mg covered by ∼32nm Pd (Type B in Figure 2.1.1 and Table 2.1.2). These curves were obtained by electro-chemical loading with in-situ optical microscopy and were constructed with the procedure introduced in paragraph 2.2.3. In the first portion of the curves, the electromotive force (EMF) at equilibrium increases with each applied current step. After this first region the electromotive force at equilibrium becomes constant, indicating that the Magnesium
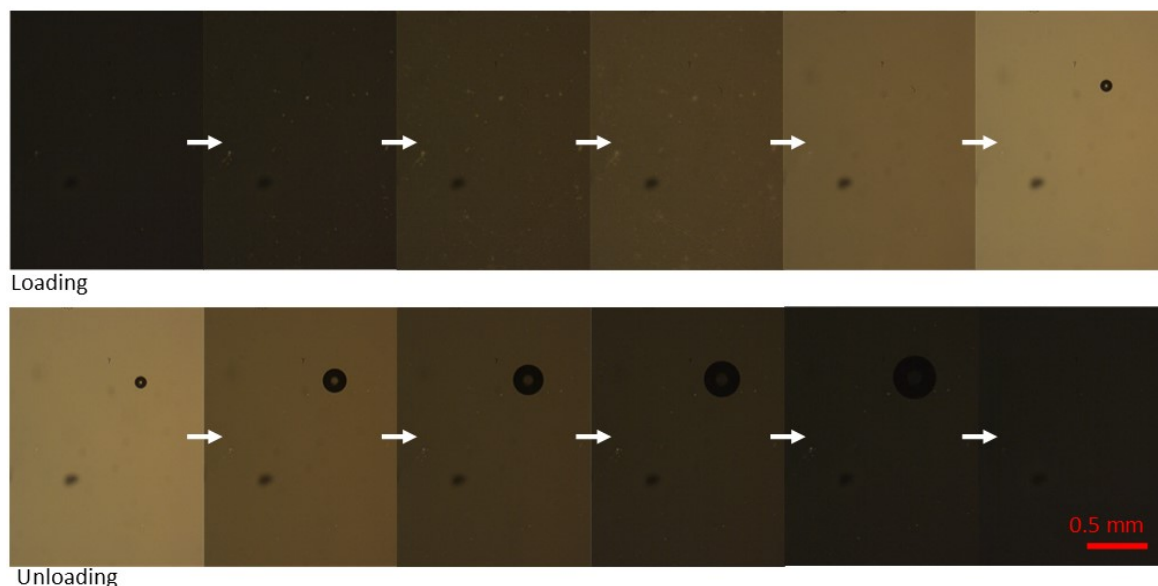
FIGURE 3.2.2. Images of the film during hydrogen loading and unloading. The images were recorded with a 10x magnification.

hydride phase is forming and that it is in equilibrium with the solid solution phase. The formation of the hydride is accompanied by an increase in the film's transmittance, as can also be seen in some images of the film in Figure 3.2.2. When the applied current is reversed for hydrogen unloading, we see a decrease in the equilibrium EMF followed by a plateau and finally by a portion were the EMF decreases again with each current step. The curves exhibit a strong hysteresis: the plateau during hydrogen loading is at 0.343V, while the one during hydrogen unloading is at 0.201V.

The isotherm whose concentration axis is evaluated from the film's transmittance (right box in Figure 3.2.1) is a closed curve. This means that, after hydrogen unloading, the film has returned to its original transmittance and so to the original hydrogen content, as can also be observed in Figure 3.2.2. The loading and unloading plateaus are in fact found in the same portion of the x-axis, approximately one above the other. The second isotherm, where the concentration axis is calculated directly from the current pulses according to equation 2.2.1, appears different: the curve is open and the unloading plateau is much smaller than the loading plateau. The different shape of the two isotherms can be understood considering the behaviour of the electrolyte during hydrogen loading. Due to the necessary high driving voltages, a high volume of hydrogen is created at the sample's surface, part of which desorbs from the surface and creates bubbles in the electrolyte instead of being absorbed by the sample. The creation of bubbles thus causes an overestimation of the hydrogen concentration during loading, leading to unphysical values of the concentration inside the sample. We know in fact that the concentration in the magnesium hydride (MgH_2) phase should not be higher than two hydrogen atoms per magnesium atom: the x-axis is therefore to be taken as an apparent hydrogen concentration. At the same time, the width of the unloading plateau is $\Delta c_H \simeq 1H/Mg$, which is a reasonable value and indicates that the problem of bubble

formation does not affect the concentration calculated during hydrogen unloading. The plateau for Palladium hydride formation would have been visible at higher concentrations. However, the film could be kept inside the electrolyte only for a limited amount of time before being damaged: this means that it was not always possible to record loading and unloading plateaus for both Magnesium and Palladium.

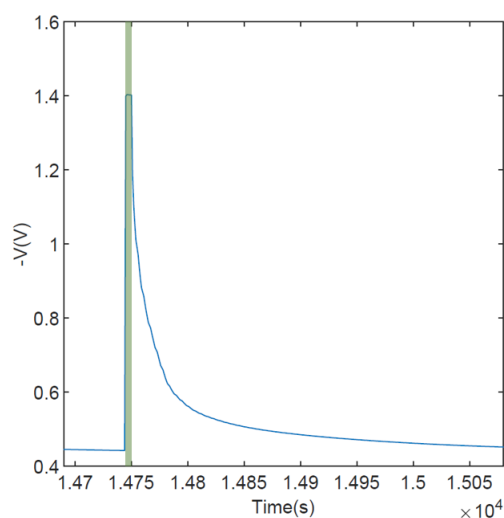## 3.3. EMF curves and patterns during Magnesium hydride formation

FIGURE 3.3.1. EMF measured by the reference elcetrode during Pd hydride formation for a film of type C ($\sim$ 39 nm Mg, see Figure 2.1.1). The green area marks the interval where an external voltage was applied using the voltage generator. After this peak, the current relaxes exponentially to its plateau value. The real value of the voltage would be negative in agreement with the cyclic voltammetry results (Figure 3.1.1), here however the inverse of the voltage is shown for an easier visualization of the plots.

During electrochemical hydrogen loading, the electromotive force (EMF) in the cell is continuously recorded at the reference electrode. This is necessary to construct the isotherm curves, whose y-axis is given by the recorded EMF once a stable value is reached after each current pulse. Even though they are not needed for the isotherms, the voltages between the current pulse and the equilibrium condition can provide further information on the system's behaviour.

Figure 3.3.1 represents the typical curve during Palladium hydride formation. The peak highlighted in green indicates that we are directly applying a potential in the cell using the voltage generator (by activating the timer, see the circuit in Figure 2.2.1); the value at this peak provides the driving force for water electrolysis and hydrogen absorption in the sample. After a certain interval, the timer is deactivated so we are not applying any external voltage. At this point, the voltage measured by the reference electrode decreases exponentially until it reaches a stable value around 0.45V. This behaviour was observed during Pd hydride formation for all the examined samples.
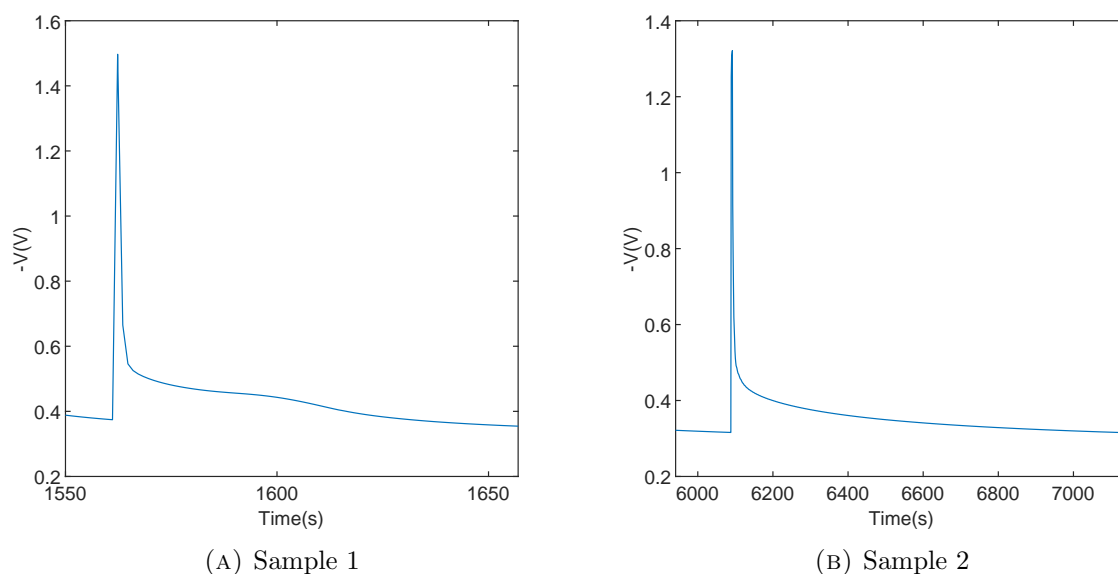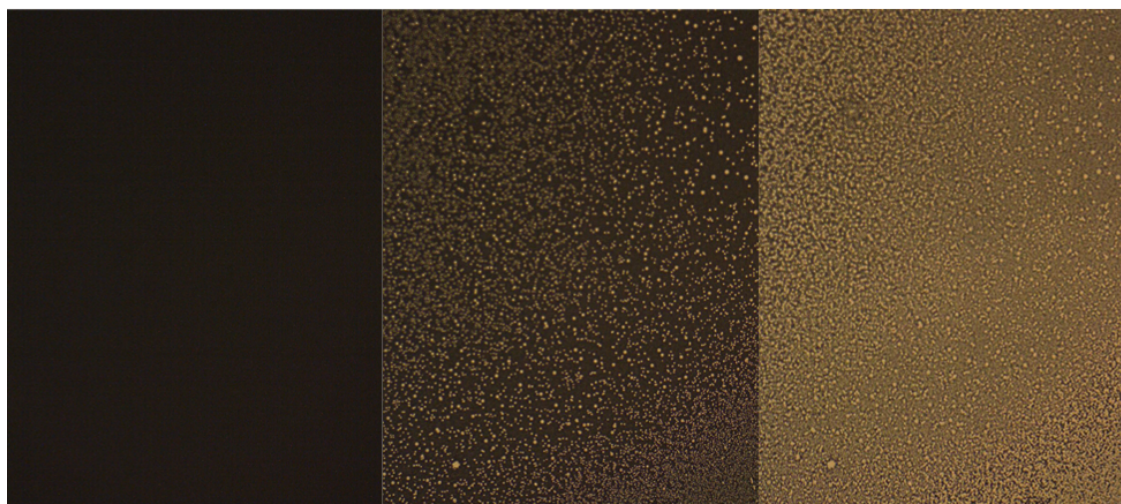
(A) Sample 1

(B) Sample 2

FIGURE 3.3.2. Comparison of two EMF curves during Mg hydride formation. (A) A higher external voltage was applied and the curve exhibits two plateaus. The first plateau is around 0.45V, the same value observed during Palladium hydride formation. (B) A lower external voltage was applied, the curve shows an exponential relaxation to equilibrium and there is no plateau around 0.45V.

Different behaviours were observed during Mg hydride formation. Some samples exhibited a two-plateau curve: after the peak corresponding to an applied external voltage the recorded EMF decreased to a first plateau, and only after that the voltage decreased again to reach a final stable value. Some samples instead exhibited a EMF curve similar to the one of Pd hydride formation, with a simple exponential relaxation to the plateau value. Two examples of these different behaviours are reported in Figure 3.3.2; the sample exhibiting a two-plateau curve was labelled as Sample 1, the sample with an exponential curve was labelled as Sample 2. Sample 1 had a ∼15nm Mg layer, while Sample two had a ∼39nm Mg layer. The different shapes of the EMF curves during Mg hydride formation where also accompanied by different patterns in the pictures recorded with the optical microscope. As represented in Figure 3.3.3, the double-plateau curve is characterized by a uniform increase of the film's brightness after each loading step. On the other hand, the exponential curve is characterized by the appearance of quite large circular hydrides that expand after each loading step, to eventually cover the whole surface.

These different behaviours can be understood considering the role of the driving force to hydride nucleation and of the Magnesium hydride blocking layer. We notice in fact that the larger hydrides and single plateau curve are related to a lower applied voltage (around 1.4V), which generates a lower driving force. At the same time, the double-plateau curve and the uniform brightness variation, which is caused by very small hydride

Sample 1, high driving force

Sample 2, low driving force

FIGURE 3.3.3. Two different patterns observed during Magnesium hydride formation. These patterns are related to different shapes of the recorded EMF curves between the loading voltage and the equilibium condition. A unifrom variation of the film's brightness comes with a two-plateau curve, while circular structures at the surface comes with an exponential curve (cfr Figure 3.3.2).

precipitates, are observed for an higher applied voltage (around 1.5V). Further details will be given in the Discussion chapter.

3.4. Thickness effects with electrochemical hydrogen loading

Figure 3.4.1 represents the isotherm curves measured with electrochemical hydrogen loading for the three different Mg-Pd samples introduced in paragraph 2.1.2. The samples were composed by Magnesium layers of different nominal thicknesses – ∼13nm, ∼26nm
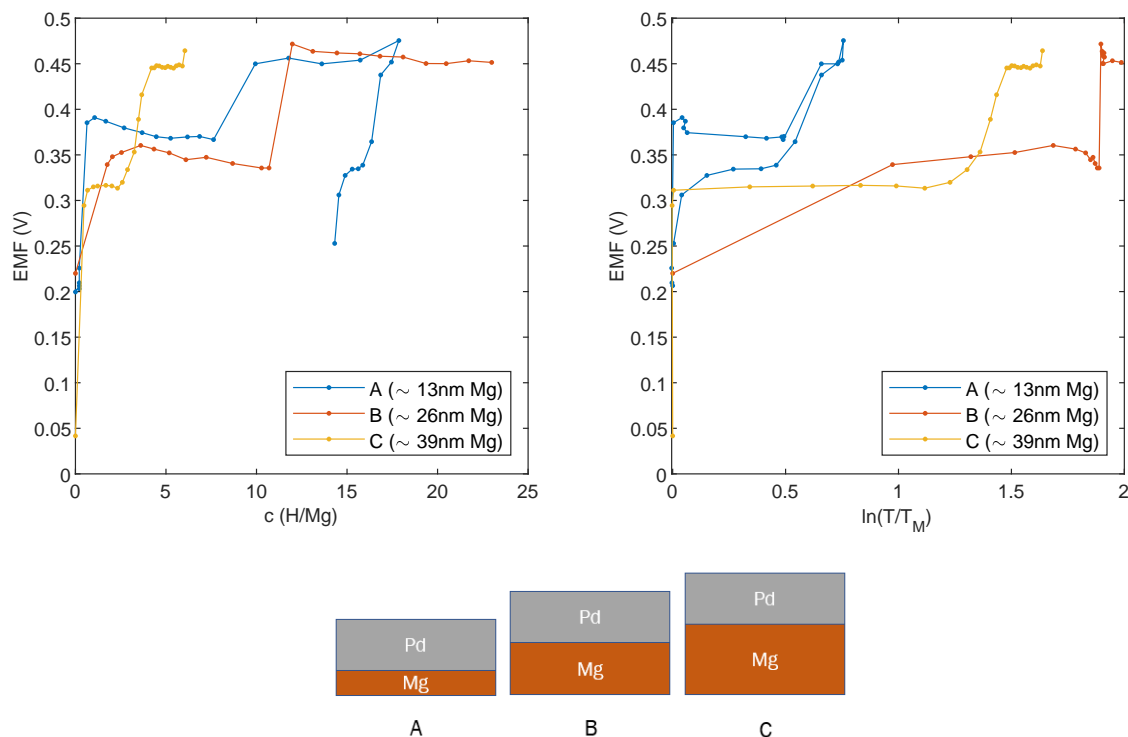
FIGURE 3.4.1. Isotherm curves obtained via electrochemical hydrogen loading for three different Mg-Pd samples (A,B and C in the figure). All samples had the same Pd thickness and different thicknesses of the Mg layer (13nm, 26nm and 39nm as also reported in Table 2.1.2). We can see that, while the Pd hydride formation plateau is always in the same position, the Mg hydride formation plateau moves to higher EMF values as the film gets thinner.

TABLE 3.4.1. Central value of the Mg hydride formation plateau calculated from electrochemical and gas phase hydrogenography for three different Mg-Pd samples. All samples had the same Pd thickness and different thicknesses of Mg.

Sample	nominal d_{Mg}	EMF plateau (V)	pressure plateau (mbar)
A	13 nm	0.315 ± 0.002	1.0 ± 0.2
B	26 nm	0.347 ± 0.009	1.5 ± 0.4
C	39 nm	0.375 ± 0.009	-

and ∼39nm – always covered by a ∼32nm layer of Palladium (see Table 2.1.2 for more details). As in previous results, two sets of isotherms were plotted with different x-axis: one from direct measurements of the concentration and one from the logarithm of the film's transmittance. All the measured curves exhibit two loading plateau regions. The one at lower concentrations is related to the formation of the hydride phase in the Mg

layer, while the one at higher concentrations corresponds to hydride formation in the Pd layer. The Pd loading plateau is at the same voltage for all the measured samples, as we expect since the Pd thickness was always kept constant. On the contrary, the position of the Mg loading plateau varies with the layer's thickness: the 13nm film has the highest plateau, the 26nm one is intermediate and the 39nm film shows the lowest plateau. The plateaus' central values are reported in Table 3.4.1; this was necessary since, as we can observe in Figure 3.4.1, the plateaus are not perfectly horizontal but they exhibit a downward inclination.

The acquisition of the full loading and unloading curve was possible only for the thinner sample. In this case, similarly to what was found in paragraph 3.2, the unloading plateau has a reasonable value of $\Delta c_H = 1.3 H/Pd$ and an hysteresis is observed during Mg hydride dissolution. In the other cases damage from the electrolyte prevented the measurement of hydrogen unloading.

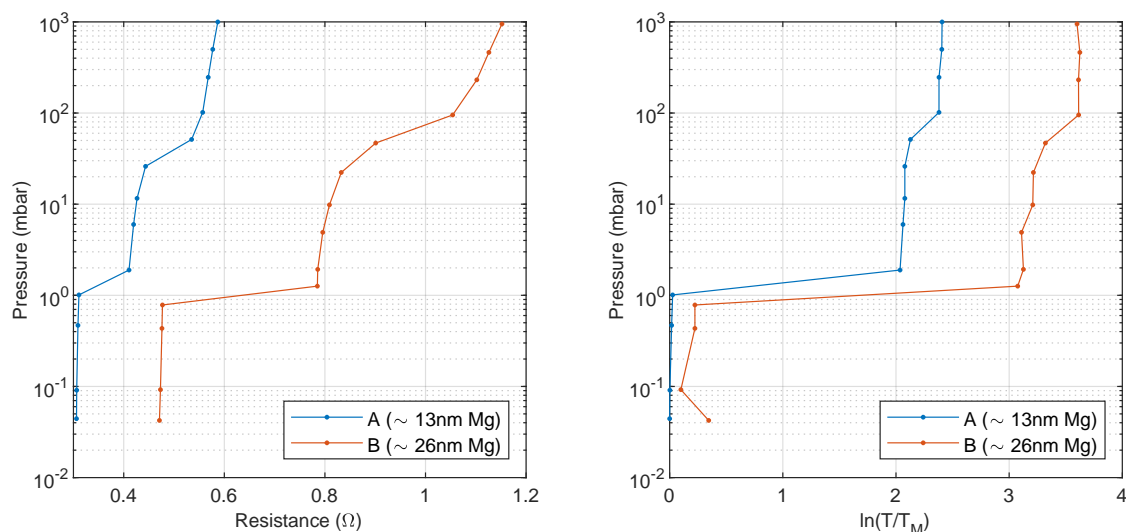## 3.5. Thickness effects with gas-phase hydrogen loading

FIGURE 3.5.1. Isotherms measured via gas-phase hydrogen loading for two Mg-Pd samples of different Mg thicknesses: Sample A with 13nm Mg and Sample B with 26nm Mg. The concentration axis is given by the sample's resisatnce on the left and by its optical transmittance on the right.

Figure 3.5.1 reports the isotherm curves obtained from gas-phase hydrogen loading for films of the type A (13nm Mg, 32nm Pd) and B (26nm Mg, 32nm Pd). As explained in paragraph 2.3, the concentration was determined from the sample's resistance and optical transmittance, while the y-axis was built using the logarithm of the hydrogen gas pressure, which is proportional to its chemical potential. Similarly to electrochemical measurements, we observe two plateaus in the loading curves: the first one related to Mg hydride formation and the second one related to Pd hydride formation. Table 3.4.1

shows that, in agreement with the results from electrochemical loading, the pressure plateau for the thinner film is slightly higher than the one of the thicker film, even tough the achieved precision is barely sufficient to properly distinguish the two values. A more precise result could be obtained by applying smaller pressure steps when measuring the curves, this would however slow down the measurement process because of the slow kinetics of the system, especially at pressures close the the plateau's edge.
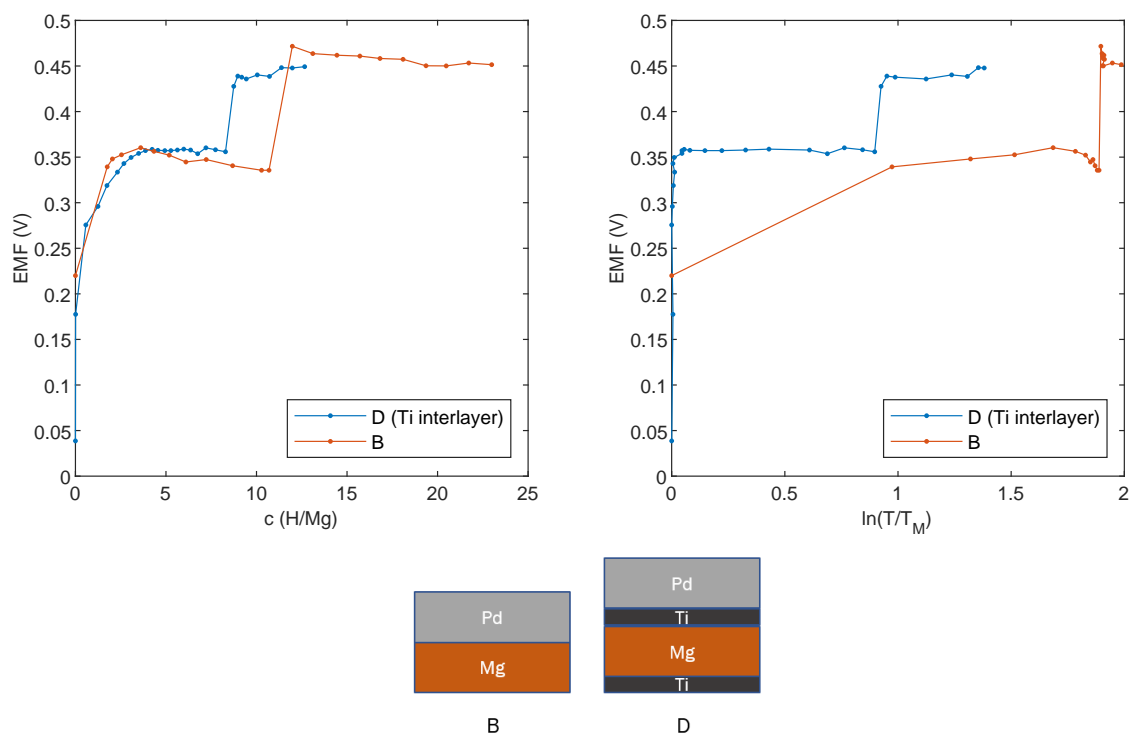
3.6. Effect of a Titanium interlayer

FIGURE 3.6.1. Electrochemical isotherms of two samples of Type B (26nm Mg, 32nm Ti) and of Type D (equal to Type B but with two 10nm Ti layer surrounding the Mg one). Mg and Pd loading plateaus are in the same position for both samples, indicating a negligible effect of the Ti interlayer.

Figure 3.6.1 shows the electrochemical isotherms for two samples of Type B and D. The two samples were built with the same thickness of the Mg and Pd layers (26nm Mg and 32nm Pd, see Table 2.1.2). However, the Type D sample had two extra 10 nm layers of Titanium surrounding the Magnesium layer. The Ti interlayer separates the Mg and Pd layers, thus preventing the formation of alloys between the two metals. Moreover, as was shown in paragraph 1.6, Ti has a very low solubility in Mg and does not form intermetallic compounds. This interlayer thus excludes alloying effects from the measured isotherms, with respect to Magnesium hydride formation. As we can see in Figure 3.6.1, the position of the EMF plateaus does not vary when the Ti layer is inserted. This

indicates that alloying does not play a major role in the Mg hydride formation potential for films around 30nm thick; an effect may be detected by considering thinner Mg films.

4. Discussion

This chapter discusses and interprets the previously reported results, focusing on the two patterns observed during Magnesium hydride formation (paragraph 4.1) and on thickness effect (paragraph 4.2). Paragraph 4.3 concludes the chapter with a comparison and evaluation of the two methods used for hydrogen loading.

4.1. Patterns during hydride formation and the driving force

The two different behaviours observed in paragraph 3.3 during Magnesium hydride formation can be understood considering the role of the blocking layer and its relation to the applied driving force. The double-plateau curve that was sometimes observed during Magnesium hydride formation is related to the presence of the blocking layer at the interface between Magnesium and Palladium. The Mg hydride blocking layer prevents hydrogen from quickly diffusing from the Pd to the Mg layer. Instead, hydrogen is briefly blocked in the Pd layer where it forms Palladium hydride with variable concentration, creating the first voltage plateau at 0.45V (the same value observed during Pd hydride formation, as can be seen in Figure 4.1.1). Then, hydrogen diffuses through the blocking
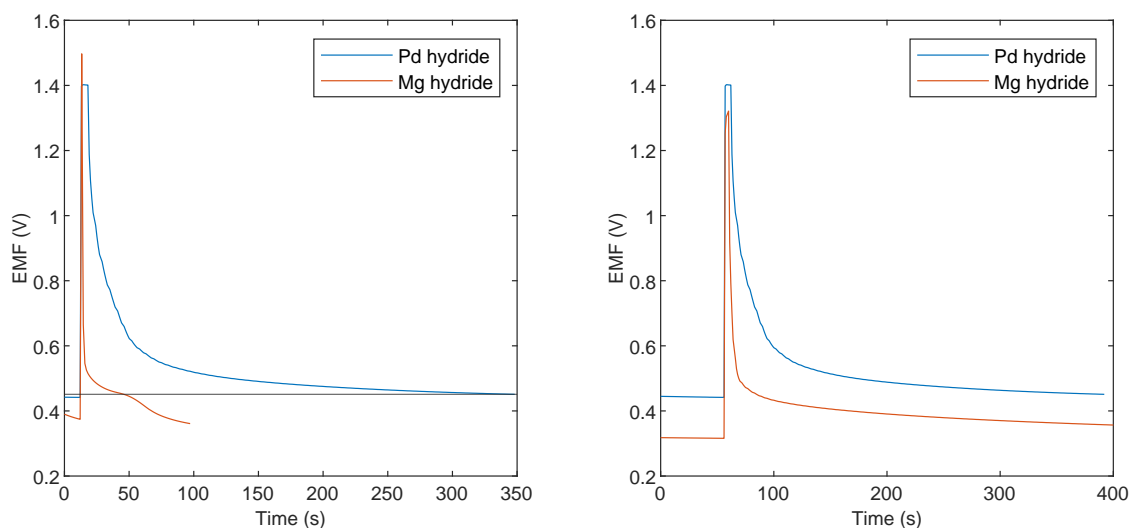
FIGURE 4.1.1. Electromotive force during Magnesium hydride formation for the two different observed patterns, compared with the curve for Palladium hydride formation. We see that during Palladium hydride formation the EMF curve settles to a higher value. However, the first plateau during Magnesium hydride formation, that arises for an higher applied voltage, is in the same position as the Pd hydride formation plateau. On the contrary, the curve with a lower applied voltage only exhibits one plateau during Mg hydride formation.

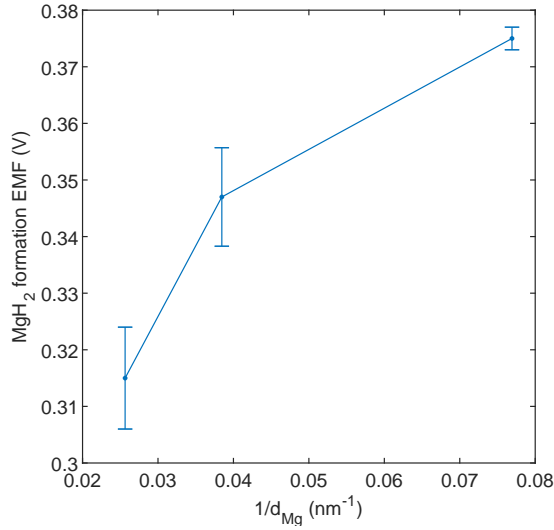FIGURE 4.2.1. Relation between the central value of the Mg hydride formation plateau, taken form the curves in Figure 3.4.1, and the inverse of the film's nominal thickness. We can see that the EMF plateau increases as the film gets thinner.

layer to create Magnesium hydride and the voltage drops to its final value. The time duration of the first plateau increases after each loading step, which is compatible with the growth of the blocking layer's thickness. The two-plateau curve was observed in samples where a higher driving voltage was applied, with values around 1.5V as we can observe in Figure 3.3.3. A higher applied voltage will produce a higher hydrogen concentration at the sample's surface, leading to a higher driving force for hydride formation. The high driving force creates a large number of small circular hydride precipitates all very close to each other, leading to a uniform variation of the recorded pictures' brightness (see Sample 1 in Figure 3.3.3). On the contrary, a lower applied voltage of around 1.4V leads to the creation of hydrides that are larger and further apart, and can even be observed with the optical microscope (see Sample 2 in Figure 3.3.3). This delays the creation of the blocking layer and in fact the additional plateau at 0.45V is not present in the recorded EMF (see Figure 4.1.1).

4.2. Thickness effects

The downward orientation of the EMF plateaus in Figure 3.4.1 can be explained by stress relaxation mechanisms – such as the creation of dislocations and defects – that can lower the system's free energy as more hydrogen is introduced in the sample, in a mechanism opposite to the one introduced in paragraph 1.4.3 where a growth of hydrogen concentration without stress relaxation increases the elastic energy and thus the total free energy of the system, leading to an upward plateau.

Figure 4.2.1 shows the central value of the EMF during Mg hydride formation as a function of the inverse nominal thickness of the Mg layer d_{Mg}. We can see that the plateau potential is roughly inversely proportional to the film's thickness; this could depend on

the interface energy between the hydride and the substrate or the Pd layer, which is more relevant in thinner films due to their higher surface-to-volume ratio (see paragraph 1.4.1). In that case we should observe a linear relation between the voltage plateau and $1/d_{Mg}$ (see equation 1.4.6), which is however difficult to assess in the presented data, even though the general trend is respected. Three data points are obviously not sufficient to evaluate a possible linear correlation; further studies should consider a larger pool of data to eventually fit the distribution and extract information such as the interface energy. Also, the plotted thickness is only a nominal value calculated from the deposition rate of the source for different targets. This value could however fluctuate as the samples are created: a more precise result could be obtained by introducing a scale to have a real-time measurement of the achieved thickness.

4.3. Evaluating and comparing electrochemical and gas-phase loading

One of the main objectives of this work was to devise a routine for controlled electrochemical hydrogen loading in Mg-Pd thin films, using KOH as an electrolyte. This allowed the measurement of consistent loading and unloading isotherms across a number of different samples. The measured EMF values during hydride formation seem reliable as all samples with the same thickness of Mg and Pd exhibited a plateau at the same voltage. Moreover, the measured values are compatible with the results from previous studies with similar samples in KOH [23]. However, one of the main advantages of the electrochemical loading technique, that differentiates it from the gas-phase loading, should be the ability to directly calculate the hydrogen concentration from the applied current pulses. Due to the characteristics of the electrolyte this was only possible during hydrogen unloading, but not during hydrogen loading. Therefore, if we only consider the construction of isotherms, electrochemical hydrogen loading in KOH brings the same information as gas-phase loading: a quantity proportional to the chemical potential and an indirect measurement of hydrogen concentration in the sample. A precise measurement of the concentration also during hydrogen loading might be achieved in the future using a different electrolyte or somehow estimating the amount of hydrogen that creates bubbles on the sample's surface instead of being absorbed.

Despite yielding similar information, the main difference between the two techniques lays in the way hydrogen is introduced in the sample. In electrochemical loading a set quantity of hydrogen is created at the sample's surface, based on the intensity and duration of the applied current pulse: we are therefore creating a closed system with a limited quantity of hydrogen. After the hydrogen has entered the sample and created the metal hydride, the Nernst potential in the electrochemical cell – which is proportional to chemical potential – is measured. So we directly control the concentration of hydrogen and measure the quantity proportional to the chemical potential. On the contrary, during gas-phase hydrogen loading the quantity we directly control is the hydrogen pressure, whose logarithm is proportional to the chemical potential. After the system has reached equilibrium we then measure the hydrogen concentration from the film's transmittance or resistance. Due to the small volume of the sample compared to the hydrogen gas, we are creating an open system with a virtually infinite hydrogen reservoir. The quantity we actually measure is not the chemical potential at equilibrium, but rather the chemical potential that is necessary to start the hydride formation reaction. This could

be misleading when there are potential barriers to the nucleation of the hydride, which would require a higher driving force to start hydride formation. It might also mean that it is not possible to measure intermediate steps in the pressure plateau: once the nucleation barrier is surpassed, due to the high availability of hydrogen, the whole sample will transform in the hydride phase before reaching an equilibrium condition.

Both techniques have their advantages and disadvantages, and should be chosen on the basis of the desired outcomes. As was shown in paragraph 3.3, the acquisition of the potential in the electrochemical cell brings more information on the behaviour of the system during hydrogen absorption; for example, from the EMF curves we can see whether the Mg hydride blocking layer is present at the Mg-Pd interface. Other advantages of the electrochemical method are given by the easier to assemble and less expensive experimental setup. Common electronic instruments that can be found in every laboratory and an optical microscope are sufficient, opposed to the UHV system with a turbomolecular pump and several vacuum gauges needed for gas-phase loading. The employed electrochemical cell was custom-made to fit with the rest of the setup and with the sample's dimension, but it was still based on cheap common materials. Another advantage of this technique is that the high driving force makes the process of hydrogen absorption and hydride formation significantly faster than in gas-phase loading. The main disadvantage of this technique is that each sample can be measured just one time because of the damage caused by the electrolyte, whereas the samples are completely intact after gas-phase hydrogen loading.

Conclusions

The objective of this work was to study hydride formation in Pd-covered Magnesium thin films. The controlled loading of hydrogen was performed with two methods: via electrochemical reactions in KOH and from the gas phase. While gas-phase loading is an established technique, electrochemical loading in KOH required preliminary studies to optimize the experimental setup and measuring routine. Cyclic Voltammetry experiments with in-situ optical microscopy clarified the electrochemical reactions involved in hydrogen loading and unloading, and indicated the optimal driving voltage necessary to start these reactions while minimizing the creation of a Magnesium hydride blocking layer. The experimental setup for electrochemical hydrogen loading was then designed to directly control the applied voltage. With this setup it was possible to measure reliable loading and unloading isotherms for Magnesium thin films. When working with electrochemical loading, the isotherms were built by measuring the Nernst potential inside the electrochemical cell, which is proportional to the hydrogen chemical potential. At the same time, the concentration was evaluated directly from the applied current and indirectly from the film's transmittance. The formation of the hydride phase in Magnesium and Palladium was then observed as a potential plateau in the acquired isotherms.

Using optical in-situ microscopy during electrochemical loading, two different patterns for Magnesium hydride formation were observed. On the one hand, lower driving forces were associated to the appearance of large hydride nuclei. In this case, the recorded voltages suggest a direct loading of the Magnesium layer, without the formation of Palladium hydride. On the other hand, higher driving forces were related to a uniform variation of the film's transmittance, which can be caused by hydride nuclei whose size is smaller than the microscope's resolution. In this case, the recorded voltages indicate that Palladium hydride is briefly formed in the top layer before the formation of Magnesium hydride.

To investigate the role of alloying, the isotherms of a simple Mg-Pd sample (∼26nm Mg and ∼32nm Pd) were compared to the ones of a second sample where the ∼26nm Mg layer was surrounded by two 10nm Titanium interlayers. The Ti interlayers prevented alloying between Mg and Pd; however, their presence did not affect the position of the loading plateau, indicating that for this thickness alloying does not play a major role in determining the equilibrium potential for hydride formation.

To study thickness effects three types of samples were prepared, consisting of a Magnesium layer of varying thickness (∼13nm, ∼26nm and ∼39nm) covered by a ∼32nm Palladium layer. Loading isotherms were measured for all three types of samples, revealing an inverse relation between the position of the Magnesium hydride formation plateau and the film's thickness. Pressure-concentration isotherms for the ∼13nm and

$\sim$26nm Mg films were also measured with gas-phase loading and the relative position of the pressure plateaus was consistent with the results from electrochemical loading.

Bibliography

[1] Commission to the European Parliament, the Council, the European Economic and Social Committee and the Committee of Regions. The european green deal, 2019.

[2] John O Abe, API Popoola, Emmanueal Ajenifuja, and OM Popoola. Hydrogen energy, economy and storage: review and recommendation. *International journal of hydrogen energy*, 44(29):15072–15086, 2019.

[3] Commission to the European Parliament, the Council, the European Economic and Social Committee and the Committee of Regions. A hydrogen strategy for a climate neutral europe, 2020.

[4] Andreas Züttel. Materials for hydrogen storage. *Materials today*, 6(9):24–33, 2003.

[5] Volodymyr A Yartys, Mykhaylo V Lototskyy, Etsuo Akiba, Rene Albert, VE Antonov, Jose-Ramón Ares, Marcello Baricco, Natacha Bourgeois, CE Buckley, JM Bellosta von Colbe, et al. Magnesium based materials for hydrogen based energy storage: Past, present and future. *international journal of hydrogen energy*, 44(15):7809–7859, 2019.

[6] R. Kirchheim and A. Pundt. 25 - hydrogen in metals. In David E. Laughlin and Kazuhiro Hono, editors, *Physical Metallurgy (Fifth Edition)*, pages 2597–2705. Elsevier, Oxford, fifth edition edition, 2014.

[7] Yuh Fukai. *The Metal-Hydrogen System: Basic Bulk Properties*, volume 21. Springer Science & Business Media, 2012.

[8] Süleyman Er, Michiel J van Setten, Gilles A de Wijs, and Geert Brocks. First-principles modelling of magnesium titanium hydrides. *Journal of physics: Condensed matter*, 22(7):074208, 2010.

[9] LE Isaeva, DI Bazhanov, EI Isaev, SV Eremeev, SE Kulkova, and IA Abrikosov. Dynamic stability of palladium hydride: an ab initio study. *International Journal of Hydrogen Energy*, 36(1):1254–1258, 2011.

[10] A San-Martin and FD Manchester. The h- mg (hydrogen-magnesium) system. *Journal of phase equilibria*, 8(5):431–437, 1987.

[11] FD Manchester, A San-Martin, and JM Pitre. The h-pd (hydrogen-palladium) system. *Journal of phase equilibria*, 15(1):62–83, 1994.

[12] B Baranowski, S Majchrzak, and TB Flanagan. The volume increase of fcc metals and alloys due to interstitial hydrogen over a wide range of hydrogen contents. *Journal of Physics F: Metal Physics*, 1(3):258, 1971.

[13] K Zeng, T Klassen, W Oelerich, and R Bormann. Critical assessment and thermodynamic modeling of the mg–h system. *International journal of hydrogen energy*, 24(10):989–1004, 1999.

[14] Anders Andreasen. Design and building of a new experimental setup for testing hydrogen storage materials. 2005.

[15] Lennard PA Mooij, Andrea Baldi, Christiaan Boelsma, Kun Shen, Marnix Wagemaker, Yevheniy Pivak, Herman Schreuders, Ronald Griessen, and Bernard Dam. Interface energy controlled thermodynamics of nanoscale metal hydrides. *Advanced Energy Materials*, 1(5):754–758, 2011.

[16] Helmut Takahiro Uchida. *Hydrogen absorption property of nanocrystalline-magnesium films*. PhD thesis, 2015.

[17] HT Uchida, S Wagner, M Hamm, J Kürschner, R Kirchheim, Björgvin Hjörvarsson, and A Pundt. Absorption kinetics and hydride formation in magnesium films: Effect of driving force revisited. *Acta materialia*, 85:279–289, 2015.

[18] Magnus Hamm, Marian David Bongers, Vladimir Roddatis, Stefan Dietrich, Karl-Heinz Lang, and Astrid Pundt. In situ observation of hydride nucleation and selective growth in magnesium

thin-films with environmental transmission electron microscopy. *International Journal of Hydrogen Energy*, 44(60):32112–32123, 2019.

[19] JL Murray. The mg- ti (magnesium-titanium) system. *Bulletin of alloy phase diagrams*, 7(3):245–248, 1986.

[20] H Okamoto. Mg-pd (magnesium-palladium). *Journal of phase equilibria and diffusion*, 31(4):407–408, 2010.

[21] Dragica Minic. *Hydrogen Energy: Challenges and Perspectives*. BoD–Books on Demand, 2012.

[22] Gongbiao Xin, Yanyan Wang, He Fu, Guoling Li, Jie Zheng, and Xingguo Li. Promising electrochemical hydrogen storage properties of thick mg–pd films obtained by insertion of thin ti interlayers. *Physical Chemistry Chemical Physics*, 16(7):3001–3006, 2014.

[23] Giulio Bonelli. Electrochemical loading of hydrogen in mg thin films.